Drag coefficient correlation for a single burning char particle

Hancong Zhang[a], Kun Luo[a,*], Nils Erland L. Haugen[b,c], Chaoli Mao[a] , Jianren Fan[a]

[a] *State Key Laboratory of Clean Energy Utilization, Zhejiang University, Hangzhou 310027, China*

[b] *SINTEF Energy Research, Trondheim N-7465, Norway*

[c] *Dept. of Energy and Process Engineering, Norwegian University of Science and Technology Kolbjørn Hejes vei 1B, Trondheim NO-7491, Norway*

ABSTRACT

This study aims to study the effect of reactions and temperature on the drag force coefficient in the process of char combustion. For this purpose, two-dimensional fully resolved simulations are performed using the ghost cell immersed boundary method. Heat and mass transfer, together with the corresponding Stefan flow, is accounted for. Reactive particles with different reaction rates, temperatures and diameters are compared with a non-reactive adiabatic particle and a particle with outflow. For a char particle, results show that reactions tend to increase the drag force, which is converse to the effect observed for non-reactive particles with a pure outflow. This discrepancy is due to the fact that species and temperature distribution play an important role, and both of them can affect the property of the fluid. Hence, a reactive particle cannot be simplified as a particle with only outflow. Based on the current study, a new drag force correlation for a single reactive particle is obtained. The correlation shows a good agreement with the simulation results. A posterior analysis is also performed to verify the accuracy of the correlation.

Keywords: Drag force; Particle resolved simulation; Char combustion

*Corresponding author:
E-mail address: zjulk@zju.edu.cn (Kun Luo)

This is the accepted version of an article published in Combustion and Flame
http://dx.doi.org/10.1016/j.combustflame.2020.02.016

1 Introduction

In numerical simulations of multiphase flow, an accurate description of the momentum, heat and mass exchange between the fluid and the particle phase is essential. Therefore, corresponding closure models are developed to deal with the unclosed terms in the conservation equations. Moreover, the closure models may introduce errors when gaseous and heterogeneous reactions exist in this system. For instance, the drag force law for the cold state system may not be available for reactive particles, and the Nusselt number is influenced by heterogeneous reactions too. It is therefore of great importance to modify the existing isolated models to make them applicable for the reacting multiphase flow.

The interphase momentum exchange is usually described using a drag force coefficient, which is generally regarded as a function of the Reynolds number. Numerous researches have studied the mechanism of the drag force and the empirical drag correlation in a cold-state flow. For instance, Tritton [1] and S. Dennis, G.Z. Chang. [2] measured the drag force of a circular cylinder at low and high Reynolds number, respectively. Based on these experiments, some drag force correlations are proposed. The empirical drag force correlation for the spherical particle proposed by Clift et al. [3] ($C_D = 24(1 + Re_p^{0.687}) / Re_p$) is widely used for multiphase flow simulations. Another widely used drag force correlation is put forward by Schiller et al. [4]. These drag laws are of great importance for describing the momentum transfer for dilute multiphase flow simulations [5-7].

For a reactive particle, one of the difficulties to summarize a drag correlation is that the wall-normal velocity of the particle is not zero. As a result, the Reynolds number is not enough to resolve the effect of reactions on drag force. In the previous studies about the porous particles and outflow particles, the effect of non-zero wall normal velocity was discussed. For a porous particle, the fluid phase can penetrate into the particle. The fluid passing through leads to a non-zero velocity. The governing equation of the flow inside the porous particle follows the Darcy–Brinkman–Forchheimer extended model [8]. The normal component of the velocity at the rear of

This is the accepted version of an article published in Combustion and Flame
http://dx.doi.org/10.1016/j.combustflame.2020.02.016

the surface is called as “base bleed” [9]. According to Bhattacharyya et al. [10] and Yu et al. [11]’s studies, the base bleed at the rear of the cylinder has some interaction with the shear layer, making the recirculation wake detach from or penetrate into the cylinder [11]. Therefore in Wittig et al. [12]’s study, the surface ratio and particle porosity are adopted in the drag correlation to quantify the effect of the porosity.

A particle with outflow has previously been studied as a simplification of an evaporating droplet or a solid fuel particle with a Stefan flow [13]. The outflow velocity condition was implemented at the surface without considering the effect of the species. A number of studies [13-15] show that the outflow tends to reduce the drag force. For this problem, a blowing correlation [16] was introduced to quantify the effect of pyrolysis when calculating the particle response time. The Stefan flow Reynolds number was also used in the drag correlation[17]. Furthermore, in Higuera’s study [18], the definition of the drag force is modified. A gasification term was added to the drag force calculation except for pressure and the friction term. However, in Luo et al.’s study [19] about the char particle combustion, it was found that the drag force of the reactive particle is larger than the inert particle. The mechanism was not analyzed thoroughly yet.

Moreover, the properties of the flow in the vicinity of the particle also influence the drag force. Numerous studies about heated/cooled particles and supercritical multiphase flows mention this problem. Kurose et al. [20] studied the change in drag force due to the sphere being either heated or cooled. The temperature difference between particles and the inlet flow influenced the drag force. A heated particle tends to have a larger drag coefficient, and the size of the vortex ring is also influenced. Nagata et al.’s study [21] showed that the temperature changes the drag force mainly by altering the kinematic viscosity coefficient in the vicinity of the sphere.

The heterogeneous reaction is a coupled process of momentum, heat, and mass transfer. A number of studies involving surface reactions [22-24] (e.g. pulverized coal combustion and biomass combustion) and droplet evaporation [25, 26] focus on the heat and mass transfer properties on the interface, but up to now, the drag force

This is the accepted version of an article published in Combustion and Flame
http://dx.doi.org/10.1016/j.combustflame.2020.02.016

calculation of reactive particle has not been studied in detail. Heterogeneous reactions influence the drag force not only through the Stefan flow. When the momentum, heat and mass transfer occur simultaneously, the drag force may follow a more complex law. For this purpose, we perform a detailed study about how the heterogeneous and gaseous reactions influence the drag force in the process of char combustion using the ghost cell immersed boundary method.

This paper is structured as follows. The numerical method and simulation setup are described in section 2. The third section discusses the mechanism of how reactions influence the drag force. The effect of heterogeneous reactions, the gaseous reaction, and the particle temperature are studied, respectively. A new drag force correlation for single reactive particles is obtained. The fourth section is devoted to the conclusion.

2 Numerical approach and simulation setup

2.1 Numerical method

This work is based on the particle resolved study of char combustion by Luo et al. [19]. A high-order finite difference solver called the PENCIL CODE [27, 28] is used. Governing equations of gas phase and boundary conditions at the char surface are given by

$$\frac{D\rho}{Dt}+\rho\nabla\cdot u=0, \tag{1}$$

$$\frac{Du}{Dt}=\frac{1}{\rho}(-\nabla p+\nabla\cdot(2\rho\nu S)), \tag{2}$$

$$\rho\frac{DY_k}{Dt}=-\nabla\cdot J_k+\dot{\omega}_k, \tag{3}$$

$$(c_p-\frac{R}{\overline{W}})\frac{D\ln T}{Dt}=\sum_k\frac{DY_k}{Dt}(\frac{R}{W_k}-\frac{h_k}{T})-\frac{R}{\overline{W}}\nabla\cdot u+\frac{2\nu S^2}{T}-\frac{\nabla\cdot q}{\rho T}. \tag{4}$$

In the above set of equations, $D/Dt=\partial/\partial t+u\cdot\nabla$ represents the convective derivative. The traceless rate of train tensor is given by $S_{ij}=\frac{1}{2}(\partial u_i/\partial x_j+\partial u_j/\partial x_i)-\frac{1}{3}\delta_{ij}\nabla\cdot u$, while J is the diffusive flux, and $\dot{\omega}_k$ represents the reaction rate of species *k*. The reaction rates and the diffusive flux are

This is the accepted version of an article published in Combustion and Flame
http://dx.doi.org/10.1016/j.combustflame.2020.02.016

calculated according to the method mentioned in [28]. Although the energy equation uses ln$T$ instead of T, it can be easily transformed into the commonly used form by modifying $\frac{D\ln T}{Dt}$ into $\frac{1}{T}\frac{DT}{Dt}$ and using $\frac{Dp}{Dt}$ instead of expanding it based on the equation of state [29]. In the energy equation, the enthalpy is given by h while W is the molar mass of the gas phase and q is the heat flux. The ideal gas equation of state, given by

$$p = \frac{\rho RT}{\overline{W}} \tag{5}$$

is used to close the governing equations.

Due to the heterogeneous reactions at the particle surface, the boundary velocity, temperature and the species mass fraction are affected. It is essential to determine these boundary conditions properly. The mass transfer at the interface is a balance of convective flux, diffusive flux and heterogeneous reactions, which is given by

$$\bar{n} \cdot [\rho Y_k (\bar{V}_k + u_{Stefan})] = \dot{m}_k \tag{6}$$

when $\bar{n}$ represents the outward wall-normal unit vector, and $\dot{m}_k$ is the mass production rate of the k^{th} species. The diffusion velocity of the kth species, which is related to the gradient of the species mass fraction, is given by

$$\bar{V}_k = \frac{1}{X_k \overline{W}} \sum_{j \neq k} W_j D_{k,j} \nabla X_j \tag{7}$$

while u_{Stefan} represents the Stefan flow. The total species diffusion flux is zero

$$\sum_k V_k Y_k = 0 . \tag{8}$$

Based on mass transfer balance at the surface, we can calculate the Stefan flow velocity as

$$\bar{n} \cdot u_{Stefan} = \frac{1}{\rho} \sum_{k=1}^{K_g} \dot{m}_k \tag{9}$$

The boundary velocity is a combination of particle shrinking velocity and Stefan flow, which is given by

This is the accepted version of an article published in Combustion and Flame
http://dx.doi.org/10.1016/j.combustflame.2020.02.016

$$u_{IB} = u_{Stefan} + v_n = u_{Stefan} + \frac{\int_{surf} \dot{m}_c ds}{s\rho_C}. \quad (10)$$

Here s is the surface of the particle.

In this study, the temperature gradient within the particle is neglected. Therefore, the heat transfer at the interface contains the diffusive flux, radiation, reaction heat and the heat conduction outside the particle, and the particle energy balance is

$$Vc_{p,C}\frac{dT_p}{d\tau} = \int_{surf}(-\sigma\varepsilon(T_p^4 - T_0^4) + \sum_{k=1}^{K}\dot{m}_k h_k + \bar{n}\cdot\lambda\nabla T_{gas})ds \quad (11)$$

when V is the volume of the particle and T_0 represents the temperature of the incoming flow, while $c_{p,C}$ is the heat capacity of the char particle. In the radiation term, ε is the emissivity coefficient, and σ is the Stefan-Boltzmann constant. Finally, $\dot{m}_k$ and h_k are the reaction rate and enthalpy of species k, respectively. The RHS of the equation is an integral over the particle surface. In addition, the pressure gradient at the surface should be zero because of the no-penetration condition.

The improved GCIB method in our previous work [30] can be used to enforce the boundary conditions of velocity, species concentrations, temperature, and pressure. This method can reach a second-order accuracy. A more detailed description and validation of the GCIB method for char combustion can be seen in [19].

2.2 Assumptions and simplifications

In this study, a semi-global heterogeneous reaction mechanism of char conversion and a homogeneous reaction of CO oxidation are used for the simulation. The heterogeneous reactions we use are essentially from the study of Zhang et al. [30], which have also been validated in our previous study [19]. For kinetic parameters and the calculation of reaction rates we refer to our previous study [19]. The kinetics parameters of reactions are shown in Table 1.

Table 1 Kinetics Parameters of reactions

Chemical reaction		B	E (J/mol)	Reference
(R1)	$2C(s)+O_2(g)\rightarrow 2CO(g)$	1.97×10^7	1.98×10^5	Zhang et al. [31]

This is the accepted version of an article published in Combustion and Flame
http://dx.doi.org/10.1016/j.combustflame.2020.02.016

(R2)	$C(s)+CO_2(g)\rightarrow 2CO(g)$	1.291×10^{5}	1.91×10^{5}	Zhang et al. [31]
(R3)	$2CO(g)+O_2(g)\rightarrow 2CO_2(g)$	2.24×10^{12}	1.6742×10^{5}	Turns [32]

Several simplifications and assumptions are needed in our study to simplify the task and focus on the key problem. Firstly, the solver we used is fully transient, but it takes too much time to resolve the whole conversion time of the char particle. Therefore, the pseudo-steady-state (PSS) assumption [33] is utilized, according to which we can use the steady condition to represent the transient burning char particle with the same current particle condition if the characteristic times of convection and diffusion are much shorter than the conversion time of the char particle. As a result, the particle temperature and radius can be fixed, and the simulation can reach the quasi-steady state faster. Secondly, the particle is fixed in the flow field and the inlet flow is uniform, which has been a common assumption in many previous studies [34-37]. Thirdly, the gas phase only contains N_2, O_2, CO, and CO_2, and the effect of water gas shift is neglected. Kinematic viscosity is calculated using Wilke's method [38] instead of Sutherland's temperature dependence dynamic viscosity calculation [39]. The effect of species on the kinematic viscosity is, however, taken into consideration.

The drag force on the cylindrical particle contains two parts, namely the pressure and the friction contributions, as given by the two terms on the right-hand side in the equation below;

$$F_D = \int_A P dA + \int_A \tau dA \tag{12}$$

The accuracy of the immersed boundary method when calculating the drag force is validated in our previous study [30].

2.3 Simulation setup

In the simulations, a cylindrical char particle, with diameter D_p, is fixed in the domain. The computational domain has a size of $24D_p \times 16D_p$, and the position of the particle is shown in Fig. 1. The grid resolution is set as $\Delta x = 1/50D_p$. The NSCBC boundary condition is used at the incoming and outlet boundaries. Meanwhile, periodic boundary conditions are used in the spanwise direction. Parameters of the incoming

This is the accepted version of an article published in Combustion and Flame
http://dx.doi.org/10.1016/j.combustflame.2020.02.016

flow and the char particle are shown in Table 2. Different particle Reynolds numbers and particle temperatures are analyzed. The particle Reynolds number is given by

$$Re = \frac{UD_p}{\upsilon}. \tag{13}$$

Here, U and υ are the velocity and kinematic viscosity coefficient of the incoming flow. In addition, to analyze the effect of reaction rate, we arbitrarily change the pre-exponential factor (denoted by *B in* Table 2) of the heterogeneous reactions. B_0 refers to the original value of pre-exponential factor of the heterogeneous reactions. At an identical Reynolds number, different diameters cause the variation of the time scale of reactions and diffusion. For this purpose, cases with different diameters are also performed. Every case is simulated until it reaches a quasi-steady state.

Table 2 Parameters of the simulation conditions

Parameter	Values
p_0	$1.01 \times 10^5\ Pa$
Y_{O2}	23% (diluted by N_2)
T_{inlet}	1500K
Re	5, 10, 20
$T_{particle}$	1400K, 1500K, 1600K, 1800K
D_p	100μm, 200μm, 400μm
B	$0.1B_0$, $0.5B_0$, $1.0B_0$, $1.5B_0$

3 Results and Discussion

3.1 Flow pattern

As mentioned in section 2.1, the heterogeneous reactions at the surface of the particle result in a Stefan flow, which causes a nonzero normal velocity. This nonzero normal velocity changes the structure of the particle boundary layer. In some previous studies of particles with outflow [13, 14, 17, 26] and porous particles [11, 12, 40, 41], the effect of wall-normal velocity is also mentioned. As shown in Fig. 2, when positive wall-normal velocity occurs, the stagnation point at the front of the particle become detached from the surface. The position of the stagnation point depends on the incoming

This is the accepted version of an article published in Combustion and Flame
http://dx.doi.org/10.1016/j.combustflame.2020.02.016

flow and the Stefan flow.

Because of the Stefan flow, we cannot find a specific separation angle at the surface. Meanwhile, the recirculation wake structure changes. According to Bhattacharyya et al.'s study [10], the critical Reynolds number of a cylindrical particle where the separation point first occurs is about 7. This criterion is no longer valid for a cylindrical reactive particle. The Stefan flow restrains the formation of the recirculation wake. As Fig. 2 shows, the recirculation wake is detached from the particle. The critical Reynolds number where the recirculation wake occurs depends on the local Stefan flow Reynolds number, which is originally defined as

$$Re_{stefan\_local} = \frac{u_{stefan} D_p}{\upsilon}. \tag{14}$$

A larger local Stefan flow Reynolds number results in a larger critical Reynolds number.

For a reactive particle, an average Stefan flow Reynolds number over the particle surface needs to be defined. Considering it may be used in a point source particle simulation, which cannot integrate Re_{stefan} over the surface, so the average Stefan flow Reynold number is defined as

$$Re_{stefan} = \frac{D_p \int_{Surf} \sum_{k=1}^{K_g} \dot{m}_k ds}{\rho \upsilon}, \tag{15}$$

where ρ and v are the density and kinematic viscosity coefficient of the incoming flow, and $\dot{m}_c$ is the average char combustion rate on the surface (kg/m^{2}s).

In Fig. 2, the length of the wake becomes shorter and the front of the wake is further from the particle when reaction rates increase. The so-called 'base bleed' of the porous particle has the analogous effect on the recirculation wake. The formation of the recirculating wake can be explained using Leal and Acrivos's entrainment-detrainment mechanism [9]. According to the mechanism, the wake at the rear of the bluff body is formed because the fluid entrained inside the shear layer gets separated from the shear layer and reverses itself again to meet the entrainment need of the shear layer. But for a char particle or a porous particle, the wall-normal velocity meets the entrainment demand of shear layer, hence the recirculating wake is weakened.

This is the accepted version of an article published in Combustion and Flame
http://dx.doi.org/10.1016/j.combustflame.2020.02.016

3.2 Effect of reactions

In the process of char conversion, heterogeneous and gaseous reactions happen simultaneously. Not only the flow pattern is influenced, but also the fluid properties are affected because of the non-uniform temperature and species distribution around the particle. In this section, the effects of heterogeneous and gaseous reactions are analyzed. To simplify the study, in this section the particle temperature is set to be equal to the temperature of the incoming flow.

3.2.1 Heterogeneous reactions

In several previous studies, the effects of heterogeneous reactions and evaporation are simplified as a pure outflow [15, 42]. Hence, the effect of species distribution resulting from relative rate of reaction and diffusion, is neglected. In the following, a reactive particle is compared with a non-reactive outflow particle, which has the same outflow velocity profile as the reactive particle's Stefan flow.

In previous studies about outflow particles [13-15, 17], the Stefan flow tends to weaken the drag force. In these studies, the Stefan flow has little influence on the pressure but attenuates the friction. Fig. 3 compares how the drag, pressure and friction coefficients varies with the Re_{stefan} for a reacting char particle and for a non-reacting particle with outflow. For a reacting char particle, the drag force increases slightly with increasing reaction rate (i.e.; with increasing Stefan flow). This is in contrast to what is found for a non-reacting particle with outflow, where in increase in Re_{stefan} results in a *decrease* in the drag coefficient. At the same outflow Reynolds numbers, the friction coefficients of reactive particles and outflow particles are not exactly the same, and the friction coefficient of the reactive case is slightly higher. The difference in drag force is, however, mainly due to differences in the pressure contribution. The differences in the pressure contribution is due to the species profiles caused by the heterogeneous reactions. Hence, it is apparent that a particle with heterogeneous reactions cannot be simplified as just a particle with outflow.

3.2.2 Gaseous reaction

The species distribution and fluid properties are affected by the gaseous reaction.

This is the accepted version of an article published in Combustion and Flame
http://dx.doi.org/10.1016/j.combustflame.2020.02.016

This effect is seldom mentioned in previous studies of the particle drag force. The gaseous and heterogeneous reactions are coupled, which makes it more complicated to identify a universal criterion by which to describe the effect of reactions. According to the simulations presented in section 3.2.1, the species distribution becomes non-uniform and offsets the effect of outflow. Similarly, the gaseous reaction makes it more pronounced. Based on the discussion of the heterogeneous reactions, the gaseous reaction is now included to clarify its effect on the drag force.

Based on the definition of drag force (as shown in section 2.2), here we define a local pressure coefficient and a local friction coefficient to describe the distribution of the local drag force components;

$$C_{P\_local} = \frac{(p - p_{front})}{1/2\rho U^2}, \qquad C_{\tau\_local} = \frac{\nabla \cdot (2\rho\nu S) \cdot \vec{x}}{1/2\rho U^2} \tag{16}$$

where p_{front} is the pressure at the front point of the cylinder surface in the streamwise direction, and $\vec{x}$ is the streamwise unit vector. The density and the streamwise velocity of the incoming flow is given by ρ and U, respectively. In the following discussion, θ refers to the surface angle of the cylinder, and $\theta = 0$ is the front of the cylinder toward the incoming flow.

As the left panel of Fig. 4(a) shows, at the rear side of the particle, cases with gaseous reactions (B>0) have slightly larger pressure drops. According to the ideal gas state equation, the pressure is related to the density, molar mass and temperature of the gas phase.). As Fig. 5 shows, since convection dominates the transport in the vicinity of the particle, CO tends to be consumed at the rear, yielding a high temperature region at a certain distance from the particle. From the simulations, we know that the temperature difference between the boundary temperature and the particle temperature is less than 1K (within 0.067% of the particle temperature. Therefore, the non-uniformity of density and molar mass results in the remarkable pressure drop at the rear of the particles. As Fig. 6 shows, with the reaction rate increasing, the CO concentration increases at the front of the particle. The gaseous reaction consumes CO and a lower concentration occurs at the rear. With the CO_2 concentration increasing, the molar mass

This is the accepted version of an article published in Combustion and Flame
http://dx.doi.org/10.1016/j.combustflame.2020.02.016

of the mixture becomes higher and the viscosity at the surface is lower. Fig. 7 shows the density and molar mass profile around the particles. The molar mass of the gas phase shows a more distinct increase at the back side of the particle. The molar mass shows a slightly higher increase than the density and cause the increase of the pressure drop.

Meanwhile, Fig. 4 shows that the local drag due to friction is slightly different from the non-reactive particle at the front and rear of the particle, but the friction at the side of the particle is almost the same. Fig. 8 shows the normalized kinematic viscosity distribution when the kinematic viscosity is normalized using the parameter of the incoming flow. Please notice that the kinematic viscosity around the particle is lower than for the incoming flow, which is due to the species profile. The gaseous reaction leads to an accumulation of CO_2 at the rear of the particle, which results in a decreased viscosity. Besides, from Fig. 4(b), it can be seen that for $0<\theta<30°$, the friction force of a reactive particle is higher than for a non-reactive particle. Considering the lower viscosity of reactive particles, as shown in Fig. 8, the velocity gradient must be higher in this region. This may be because the streamwise velocity component of the Stefan flow in this region is opposite to the incoming flow. For the same reason, in the region of $150°<\theta<180°$ in Fig. 4, the reactive particle has a lower velocity gradient and viscosity, so the friction is lower. Meanwhile, as Fig. 9 shows, the oxidation of CO causes a high temperature region in the boundary layer, and therefore the kinematic viscosity coefficient increases. As a result, the velocity distribution is also different from that of a particle with pure Stefan flow, and the friction at the surface is affected.

In many studies on the drag force of particles with outflow [13, 14], Re_{stefan} is used as a variable to describe the change in the drag force. However, when the gaseous reaction is introduced into the system, the validity of using only this dimensionless number to predict the drag force should be verified. If we keep the particle Reynolds number fixed, the drag force must be a function of the Re_{stefan}. The symbols in Fig. 10 represent simulation results, while the solid lines are obtained using quadratic polynomial fitting. From the fitting, it can be concluded that, when the diameter is fixed, the drag force has a quadratic dependence on Re_{stefan}. However, when the diameter of

This is the accepted version of an article published in Combustion and Flame
http://dx.doi.org/10.1016/j.combustflame.2020.02.016

the particle is changed, Re_{stefan} is no longer enough to describe the drag force, and other variables must be introduced. From Fig. 10(a), we can see that the drag force of a D_p=100μm reactive particle is almost equal to that of non-reactive particle (Re_{stefan}=0), so heterogeneous and gaseous reactions can even be neglected when the diameter is relatively small. The reason is that when the diameter becomes smaller, the time scales of convection $\tau_{conv} = D_p / U$ and diffusion $\tau_{diff} = D_p^2 / D_{CO}$ both decrease, and the accumulation of products at the rear of the particle is attenuated. Fig. 11 shows the contours of Y_{CO} in the neighborhood of particles with different diameters at the same Reynolds number. For the particle with a larger diameter, CO is burnt at the surface, and the concentration become lower. The smaller particle shows higher char combustion rate, but CO tends to be transported and burnt far from the particle and cannot be quickly consumed at the surface. For the same reason, Fig. 10(b) shows that the effect of reactions is weakened in a higher Reynolds number, which is also due to the decrease in the time scale of convection.

3.3 Effect of the particle temperature

When the particle temperature is different from the incoming flow, the change of fluid properties must be taken into account. According to Kurose et al.'s study [20], the main factor of influence is the viscosity. When a reactive particle has a temperature that is different from the temperature of the incoming flow, the difference in drag is larger than a heated/cooled particle without heterogeneous and gaseous reactions. For this purpose, we compare reactive particles with different temperatures.

The incoming flow temperature is fixed (1500K), and the temperatures of reactive particles are 1400K, 1500K, 1600K, and 1800K, respectively. As Fig. 12 shows, the distribution of pressure and friction are affected simultaneously. The increasing magnitudes of pressure coefficient and friction coefficient are close. In Kurose et al.'s study [20], the pressure of the heated particle is higher than for the adiabatic particle in the region of $54° < \theta < 108°$, while the pressure is lower at the rear of the particle. They thought that it is attributed to the shift of the separation point. For a reactive particle, the effect of separation is offset by the Stefan flow. As a result, the phenomenon

This is the accepted version of an article published in Combustion and Flame
http://dx.doi.org/10.1016/j.combustflame.2020.02.016

mentioned above cannot be observed in Fig. 13. As Fig. 14 shows, the normalized kinematic viscosity is significantly influenced by the temperature, and therefore, the friction is affected. The heated/cooled particle has higher/lower friction respectively. The difference is clearly seen at around θ=90° .

3.4 Drag force correlation for a single reactive particle

According to the analysis above, reactions cause a difference in species and temperature distributions, leading to a shift of drag force, especially at the front and rear of the particle. Based on this study, a new drag force correlation that considers reactions is proposed. The result in section 3.2.1 indicates that the effect of reactions cannot be properly represented only by the Stefan flow.

For a burning char particle, the heat and mass transfer at the solid-fluid interface is related to three processes, heterogeneous reactions, the gaseous reaction and diffusion. Reaction rates of heterogeneous reactions are represented by the average char combustion rate on the surface (kg/m^{2}s). In this study, only one gaseous reaction is involved, so the reaction rate is described using the reaction rate of CO (kg/m^{3}s). When multiple gaseous reactions happen simultaneously, the selection of variables needs further study. The process of diffusion is described using the diffusion coefficient (m^2/s). According to the Buckingham π theorem [43], three more independent variables are involved without any new unit, so three more dimensionless numbers, in addition to the Reynolds number, can be obtained. Accordingly, the average Stefan flow Reynolds number Restefan, the dimensionless gaseous reaction rate (see equation below), and the diffusive Damköhler number are proposed, which are defined as

$$Re_{stefan} = \frac{\dot{m}_c D_p}{\rho \upsilon}, \quad m^*_{CO} = \frac{\dot{m}_{CO} D_p}{\rho U}, \quad Da_{diff} = \frac{\rho D_{CO}}{D_p^2 \dot{m}_{CO}} \tag{17}$$

when ρ ,U , υ are the density, velocity, and kinematic viscosity coefficient of the incoming flow, respectively. The char consumption rate due to the heterogeneous reactions is given by $\dot{m}_c$, while $\dot{m}_{CO}$ is the CO reaction rate of the gaseous reaction at the boundary of the particle. The char consumption rate can be obtained using a char combustion model such as the single-film model and double-film model.

Because the incoming temperature in all cases above is fixed, and since the range of diffusion coefficients is limited, we preliminarily use two dimensionless numbers to depict the effect of reactions. How diffusion influences this process still needs further study.

Based on the dimensionless numbers above, the original drag law can be reconstructed. Here the form of the correlation is based on Schiller et al.'s study[4]. The original drag force correlation for a sphere is

$$C_D = \frac{24}{Re}\left(1 + 0.15Re^{0.687}\right) \tag{18}$$

For the cylindrical char particle in this study, we need to change the constants of the correlation to make it applicable. Non-linear least squares fitting is used to obtain the correct constant for cold inert cylinders based on the present simulation results and Tritton's experimental results [1]. The correlation for a cylinder is given by:

$$C_D = \frac{24}{Re}\left(0.382 + 0.191Re^{0.678}\right) = 9.168Re^{-1} + 4.584Re^{-0.322}. \tag{19}$$

It can be seen from Fig. 15 that this correlation is accurate at least for Re<80.

As Fig. 10 indicates, when the reaction rate increases, C_D shows an approximately quadric dependence on Re_{stefan}. Based on the fitting results, the quadratic behavior of $\dot{m}_{co}$ is identified. Hence, the constants in Eq. (19) are replaced by quadratic polynomials, which yields the following equation:

$$\begin{aligned} C_D = &\left(a_1 Re_{stefan}^2 + b_1 m_{CO}^{*\,2} + c_1 Re_{stefan} m_{CO}^* + d_1 Re_{stefan} + e_1 m_{CO}^* + 9.168\right) Re^{-1} \\ &+\left(a_2 Re_{stefan}^2 + b_2 m_{CO}^{*\,2} + c_2 Re_{stefan} m_{CO}^* + d_2 Re_{stefan} + e_2 m_{CO}^* + 4.584\right) Re^{-0.322} \end{aligned} \tag{20}$$

For the cold non-reactive case, both Re_{stefan} and m_{CO}^* are 0, so the above equation reduces to Eq. (19), as it should do. All constants in the above equation are determined by non-linear least squares, and some small quantity terms are eliminated. In consequence, the correlation becomes

$$\begin{aligned} C_D = \frac{24}{Re}\Big[&\left(1.373Re_{stefan}^2 + 16.715m_{CO}^{*\,2} + 6.303Re_{stefan} m_{CO}^* - 0.215Re_{stefan} + 1.129m_{CO}^* + 0.382\right) \\ &+\left(-0.144Re_{stefan}^2 - 26.530m_{CO}^{*\,2} + 1.288Re_{stefan} m_{CO}^* + 0.315m_{CO}^* + 0.191\right) Re^{0.678}\Big] \end{aligned} \tag{21}$$

As Fig. 16 shows, at Reynolds numbers of 5 and 10, the tendency of how reactions influence the drag force can be captured. The adjusted coefficient of determination R^2

This is the accepted version of an article published in Combustion and Flame
http://dx.doi.org/10.1016/j.combustflame.2020.02.016

[44]of this correlation is 0.99, which shows significant accuracy. For all cases used for fitting, the maximum error occurs at Re=5, and the value is 0.3%.

To verify the correlation, a posteriori analysis is performed. Five cases at the Reynolds number of 7.5 are used. Parameters of these cases are shown in Table 3. Different reaction rates and diameters are verified. The result shows that these posterior cases are also in good agreement. The maximum error is about 1.5%, which occurs at D_p=200μm.

Table 3 Parameters of posterior cases

case	*Re*	D_p (μm)	pre-exponential factor
1	7.5	200	B_0
2	7.5	400	0
3	7.5	400	$0.5B_0$
4	7.5	400	$1.0B_0$
5	7.5	400	$1.5B_0$

Conclusively, this correlation can preliminarily be used to obtain an accurate drag force of reactive particles with low Reynolds numbers. More cases of different diameters are still needed to improve the accuracy of the correlation, and further study is needed to get a more general correlation. For cylinders with other orientation, and for spherical particles, the effect of reactions on the drag force is expected to show similar trends, but the exact correlations will not be the same as Eq. (21). This is because the reaction rates and species distributions will be different for different geometries. Nevertheless, the dimensionless numbers are still applicable to drag correlations of various geometries, which lays a solid foundation for future study. The correlation can easily be coupled with point source simulations. All parameters required to calculate dimensionless numbers can be obtained in the char combustion model, such as the single-film and double-film models.

4 Conclusions

Particle-resolved simulations are performed using the ghost cell immersed boundary method to analyze the effect of char combustion reactions on the drag force. The effect

This is the accepted version of an article published in Combustion and Flame
http://dx.doi.org/10.1016/j.combustflame.2020.02.016

of heterogeneous and gaseous reactions and the particle temperature are investigated. It can be observed that the flow patterns are changed due to the Stefan flow induced by the heterogeneous reaction. As a result, the friction force around the particle is changed. The recirculation wake becomes shorter and detaches from the particle. The heterogeneous and gaseous reactions change the species distribution around the particle and cause a considerable effect on the drag force. Particles with only heterogeneous reactions are compared with non-reacting particles with a constant outflow. The comparison shows that the effect of the Stefan flow is offset by the larger pressure drop caused by the species profile. The drag force is even slightly aggravated by the heterogeneous reactions, and this result is opposite to the effect of the Stefan flow. The gaseous reaction of CO and O_2 significantly increases the drag force. The CO_2 produced by the gaseous reaction accumulates at the rear of the particle and causes a remarkable pressure drop, which is the main reason why the drag force increases significantly. Besides, the drag force is also influenced by the temperature difference between the particle and the incoming flow. The properties of the gas phase in the boundary layer are influenced by the heat transfer at the surface. The high/low kinematic viscosity caused by the heated/cooled particle results in changes to the drag force. A char particle cannot be simplified as a particle with pure outflow when calculating the drag force. Heat and mass transfer also plays an important role. Based on the study, a drag force correlation for reactive particles is obtained. Two dimensionless numbers are proposed to represent the effect of heterogeneous reactions and gaseous reaction. The correlation shows good agreement with simulation cases. A posterior analysis is also performed to verify accuracy. The effect of reactions can be captured accurately.

Acknowledgments

This work was supported by the National Key Research and Development Program of China (No. 2017YFE0112500), the National Key Research and Development Program of China (No. 2017YFB0601805) and the European Union's Horizon 2020 research and innovation programme (No 764697).

References

[1] D.J. Tritton, Experiments on the flow past a circular cylinder at low Reynolds numbers, Journal of Fluid Mechanics 6 (1959) 547-567.

[2] S. Dennis, G.-Z. Chang, Numerical solutions for steady flow past a circular cylinder at Reynolds numbers up to 100, Journal of Fluid Mechanics 42 (1970) 471-489.

[3] R. Clift, J. Grace, M. Weber, Bubbles, drops, and particles–Academic Press, New York 510 (1978).

[4] L. Schiller, A.Z. Nauman, Ver. Deut. Ing 77, pp, (1933) 318-320.

[5] T. Hara, M. Muto, T. Kitano, R. Kurose, S. Komori, Direct numerical simulation of a pulverized coal jet flame employing a global volatile matter reaction scheme based on detailed reaction mechanism, Combustion and Flame 162 (2015) 4391-4407.

[6] M. Rieth, A. Kempf, A. Kronenburg, O. Stein, Carrier-phase DNS of pulverized coal particle ignition and volatile burning in a turbulent mixing layer, Fuel 212 (2018) 364-374.

[7] T. Brosh, D. Patel, D. Wacks, N. Chakraborty, Numerical investigation of localised forced ignition of pulverised coal particle-laden mixtures: A Direct Numerical Simulation (DNS) analysis, Fuel 145 (2015) 50-62.

[8] P. Nithiarasu, K. Seetharamu, T. Sundararajan, Natural convective heat transfer in a fluid saturated variable porosity medium, International Journal of Heat and Mass Transfer 40 (1997) 3955-3967.

[9] L. Leal, A. Acrivos, The effect of base bleed on the steady separated flow past bluff objects, Journal of Fluid Mechanics 39 (1969) 735-752.

[10] S. Bhattacharyya, S. Dhinakaran, A. Khalili, Fluid motion around and through a porous cylinder, Chemical Engineering Science 61 (2006) 4451-4461.

[11] S. Yu, P. Yu, T. Tang, Effect of thermal buoyancy on flow and heat transfer around a permeable circular cylinder with internal heat generation, International Journal of Heat and Mass Transfer 126 (2018) 1143-1163.

[12] K. Wittig, P. Nikrityuk, A. Richter, Drag coefficient and Nusselt number for porous particles under laminar flow conditions, International Journal of Heat and Mass Transfer 112 (2017) 1005-1016.

[13] M. Watanabe, J. Yahagi, Effects of Nonuniform Outflow and Buoyancy on Drag Coefficient Acting on a Spherical Particle, Journal of Flow Control, Measurement & Visualization 5 (2017) 99.

[14] R. Kurose, H. Makino, S. Komori, M. Nakamura, F. Akamatsu, M. Katsuki, Effects of outflow from the surface of a sphere on drag, shear lift, and scalar diffusion, Physics of Fluids 15 (2003) 2338-2351.

[15]

T. Jayawickrama, N. Haugen, M. Babler, K. Umeki. Effect of Stefan flow on drag coefficient of reactive spherical particles in gas flow. In: editor^editors. ICHMT DIGITAL LIBRARY ONLINE; 2018: Begel House Inc. p.

[16] M. Stöllinger, B. Naud, D. Roekaerts, N. Beishuizen, S. Heinz, PDF modeling and simulations of pulverized coal combustion–Part 1: Theory and modeling, Combustion and Flame 160 (2013) 384-395.

[17] T.R. Jayawickrama, N.E.L. Haugen, M.U. Babler, M.A. Chishty, K. Umeki, The effect of Stefan flow on the drag coefficient of spherical particles in a gas flow, International Journal of Multiphase Flow 117 (2019) 130-137.

[18] F. Higuera, Combustion of a coal char particle in a stream of dry gas, Combustion and Flame 152 (2008) 230-244.

[19] K. Luo, C. Mao, J. Fan, Z. Zhuang, N.E.L. Haugen, Fully resolved simulations of single char particle combustion using a ghost‐cell immersed boundary method, AIChE Journal 64 (2018) 2851-2863.

This is the accepted version of an article published in Combustion and Flame
http://dx.doi.org/10.1016/j.combustflame.2020.02.016

[20] R. Kurose, M. Anami, A. Fujita, S. Komori, Numerical simulation of flow past a heated/cooled sphere, Journal of Fluid Mechanics 692 (2012) 332-346.
[21] T. Nagata, T. Nonomura, S. Takahashi, Y. Mizuno, K. Fukuda, Direct numerical simulation of flow around a heated/cooled isolated sphere up to a Reynolds number of 300 under subsonic to supersonic conditions, International Journal of Heat and Mass Transfer 120 (2018) 284-299.
[22] C.R. Shaddix, E.S. Hecht, C. Gonzalo-Tirado, B.S. Haynes, The effect of bulk gas diffusivity on apparent pulverized coal char combustion kinetics, Proceedings of the Combustion Institute 37 (2019) 3071-3079.
[23] N.E.L. Haugen, J. Krüger, D. Mitra, T. Løvås, The effect of turbulence on mass transfer rates of small inertial particles with surface reactions, Journal of Fluid Mechanics 836 (2018) 932-951.
[24] S. Farazi, M. Sadr, S. Kang, M. Schiemann, N. Vorobiev, V. Scherer, H. Pitsch, Resolved simulations of single char particle combustion in a laminar flow field, Fuel 201 (2017) 15-28.
[25] M. Renksizbulut, M. Yuen, Experimental study of droplet evaporation in a high-temperature air stream, Journal of heat transfer 105 (1983) 384-388.
[26] R.S. Miller, J. Bellan, Direct numerical simulation of a confined three-dimensional gas mixing layer with one evaporating hydrocarbon-droplet-laden stream, Journal of Fluid Mechanics 384 (1999) 293-338.
[27] A. Brandenburg, W. Dobler, Pencil: Finite-difference Code for Compressible Hydrodynamic Flows, Astrophysics Source Code Library, (2010).
[28] N. Babkovskaia, N. Haugen, A. Brandenburg, A high-order public domain code for direct numerical simulations of turbulent combustion, Journal of computational physics 230 (2011) 1-12.
[29] G. Lupo, M.N. Ardekani, L. Brandt, C.J.I.J.o.H. Duwig, M. Transfer, An Immersed Boundary Method for flows with evaporating droplets, 143 (2019) 118563.
[30] K. Luo, Z. Zhuang, J. Fan, N.E.L. Haugen, A ghost-cell immersed boundary method for simulations of heat transfer in compressible flows under different boundary conditions, International Journal of Heat and Mass Transfer 92 (2016) 708-717.
[31] L. Zhang, K. Liu, C. You, Fictitious domain method for fully resolved reacting gas–solid flow simulation, Journal of Computational Physics 299 (2015) 215-228.
[32] S.R. Turns, An introduction to combustion, McGraw-hill New York1996.
[33] S. Sundaresan, N.R. Amundson, Diffusion and reaction in a stagnant boundary layer about a carbon particle. 6. Effect of water vapor on the pseudo-steady-state structure, Industrial & Engineering Chemistry Fundamentals 19 (1980) 351-357.
[34] S. Tenneti, R. Garg, S. Subramaniam, Drag law for monodisperse gas–solid systems using particle-resolved direct numerical simulation of flow past fixed assemblies of spheres, International journal of multiphase flow 37 (2011) 1072-1092.
[35] R.J. Hill, D.L. Koch, A.J. Ladd, The first effects of fluid inertia on flows in ordered and random arrays of spheres, Journal of Fluid Mechanics 448 (2001) 213-241.
[36] R.J. Hill, D.L. Koch, A.J. Ladd, Moderate-Reynolds-number flows in ordered and random arrays of spheres, Journal of Fluid Mechanics 448 (2001) 243-278.
[37] M.A. van der Hoef, R. Beetstra, J. Kuipers, Lattice-Boltzmann simulations of low-Reynolds-number flow past mono-and bidisperse arrays of spheres: results for the permeability and drag force, Journal of fluid mechanics 528 (2005) 233-254.
[38] C. Wilke, A viscosity equation for gas mixtures, The journal of chemical physics 18 (1950) 517-519.
[39] W. Sutherland, LII. The viscosity of gases and molecular force, The London, Edinburgh, and Dublin

This is the accepted version of an article published in Combustion and Flame
http://dx.doi.org/10.1016/j.combustflame.2020.02.016

Philosophical Magazine and Journal of Science 36 (1893) 507-531.
[40] P. Yu, Y. Zeng, T. Lee, H. Bai, H. Low, Wake structure for flow past and through a porous square cylinder, International Journal of Heat and Fluid Flow 31 (2010) 141-153.
[41] P. Yu, Y. Zeng, T.S. Lee, X.B. Chen, H.T. Low, Steady flow around and through a permeable circular cylinder, Computers & Fluids 42 (2011) 1-12.
[42] M. Renksizbulut, M. Yuen, Numerical study of droplet evaporation in a high-temperature stream, Journal of Heat transfer 105 (1983) 389-397.
[43] E. Buckingham, On physically similar systems; illustrations of the use of dimensional equations, Physical review 4 (1914) 345.
[44] G. Shieh, Improved shrinkage estimation of squared multiple correlation coefficient and squared cross-validity coefficient, Organizational Research Methods 11 (2008) 387-407.

This is the accepted version of an article published in Combustion and Flame
http://dx.doi.org/10.1016/j.combustflame.2020.02.016

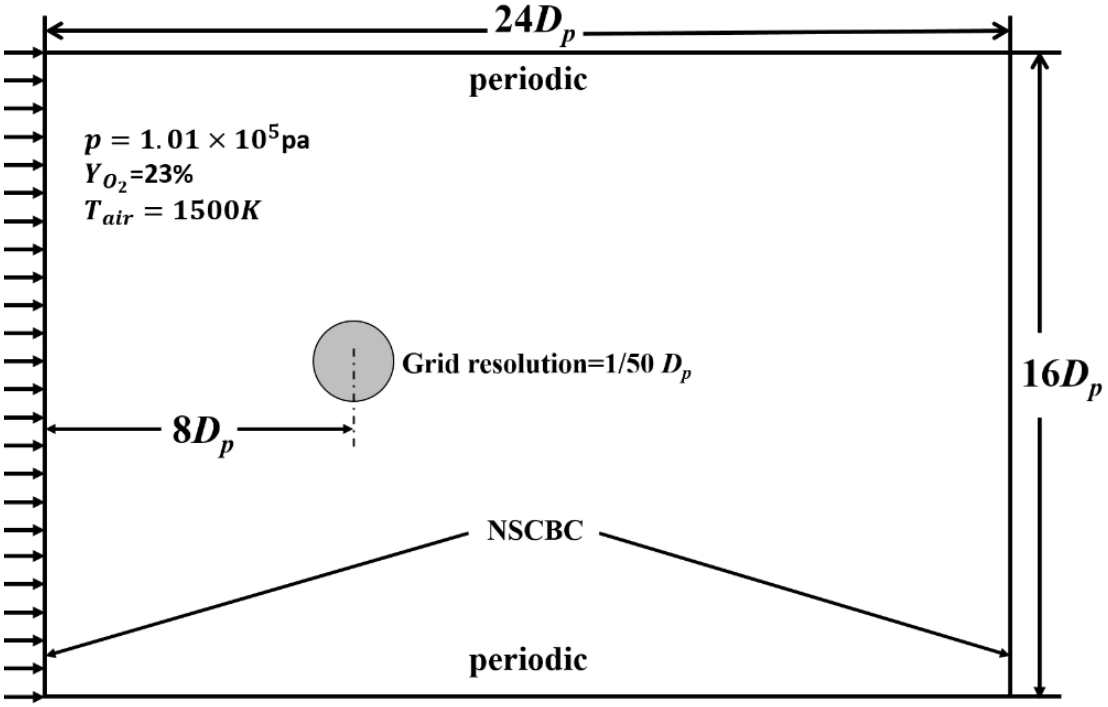

Fig. 1 Schematic of the computational domain.

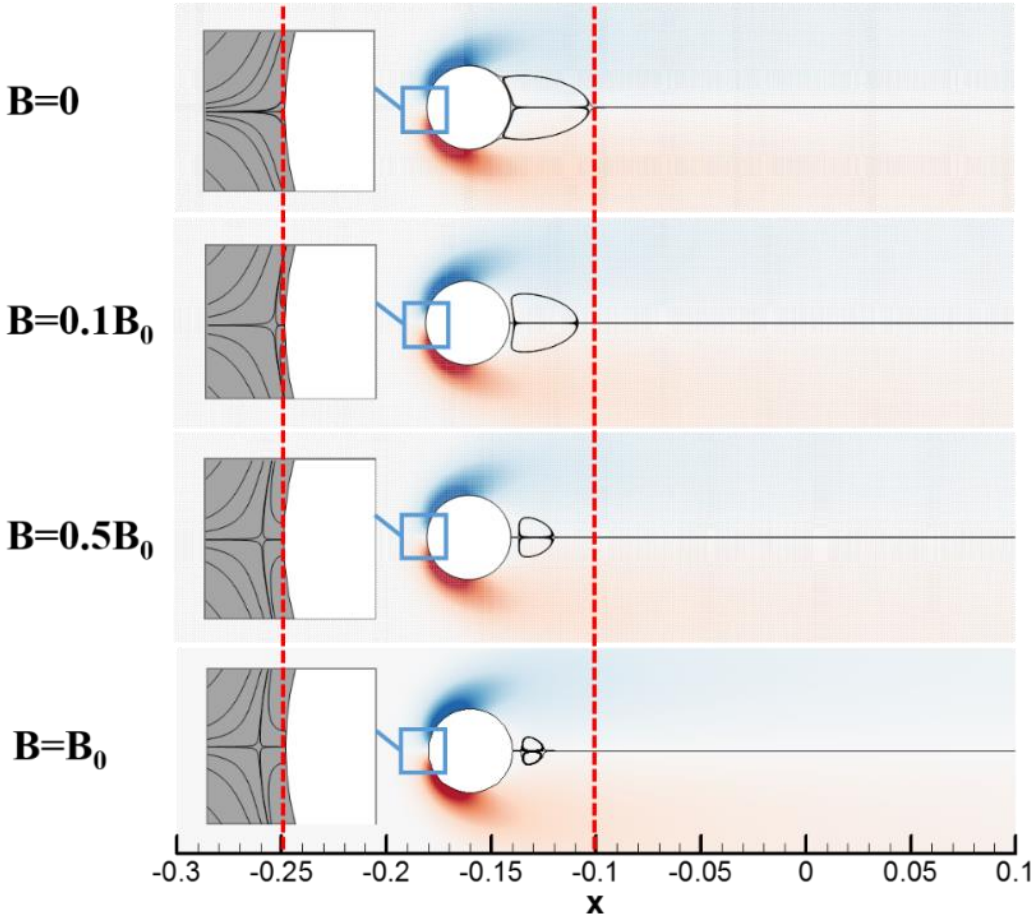

Fig. 2 The vorticity and flow pattern around the particles with different heterogeneous reaction rates ($T_{particle}$=1500K, D_p=400μm, Re=20).

This is the accepted version of an article published in Combustion and Flame
http://dx.doi.org/10.1016/j.combustflame.2020.02.016

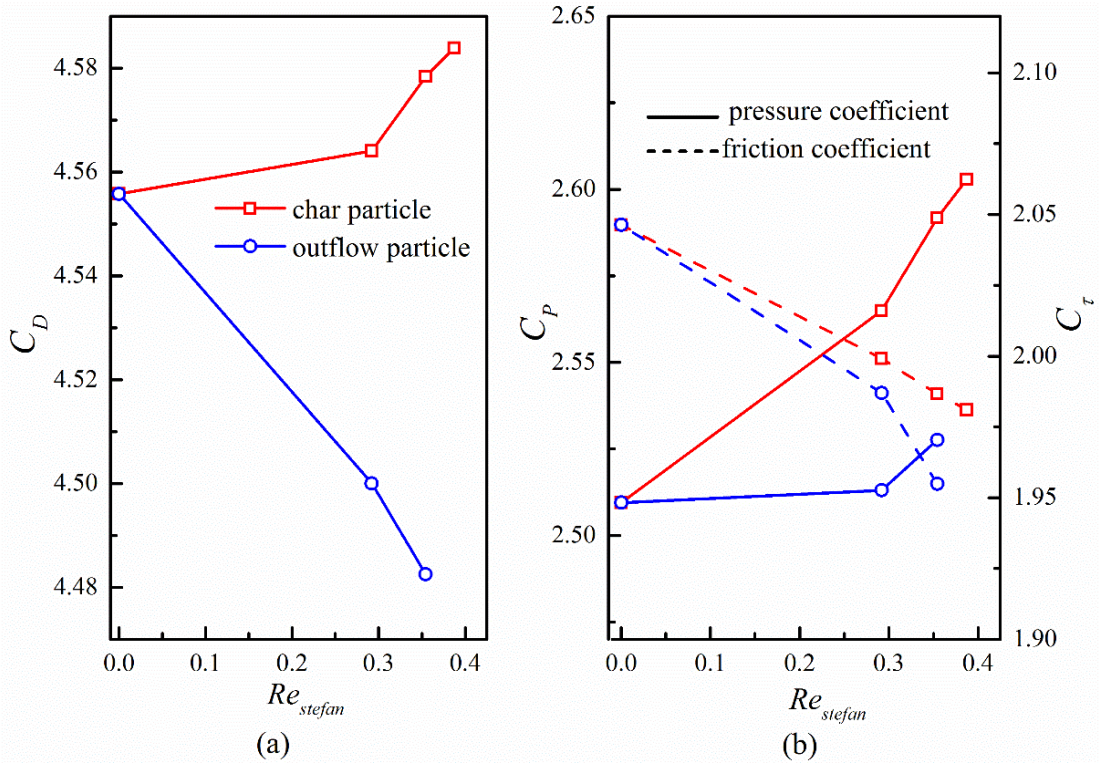

Fig. 3 The comparison of the particle with heterogeneous reactions and the particle with outflow (D_p=400μm, Re=5, $T_{particle}$=1500K for the char particle).
(a) Drag force coefficient (b) Pressure and friction coefficients.

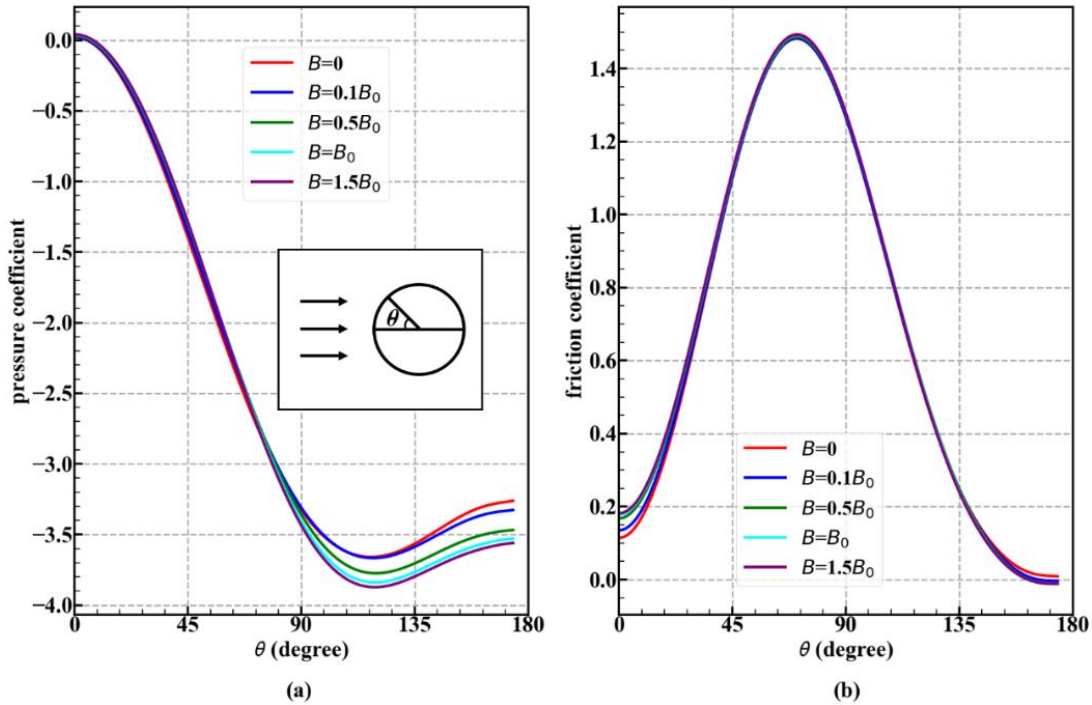

Fig. 4 Local pressure and friction coefficient distribution of particles with different heterogeneous reaction rates ($T_{particle}$=1500K, D_p=400μm, Re=5).

This is the accepted version of an article published in Combustion and Flame
http://dx.doi.org/10.1016/j.combustflame.2020.02.016

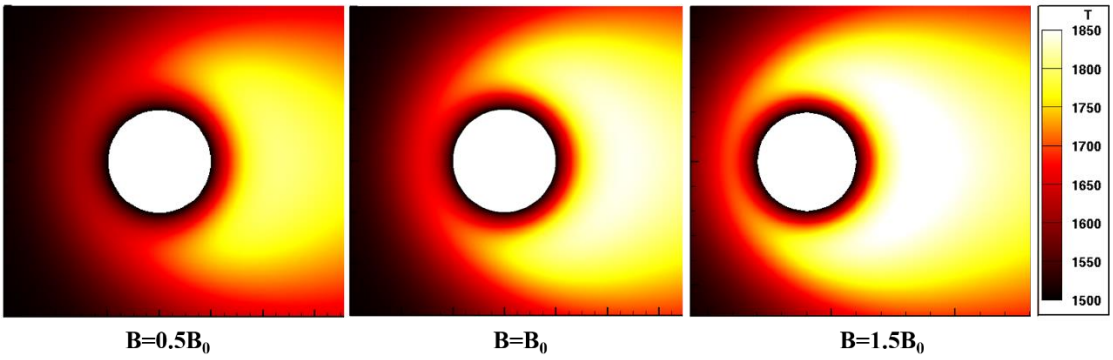

Fig. 5 Temperature contours in the neighborhood of particles with reaction rates ($T_{particle}$=1500K, D_p=400μm, Re=5)

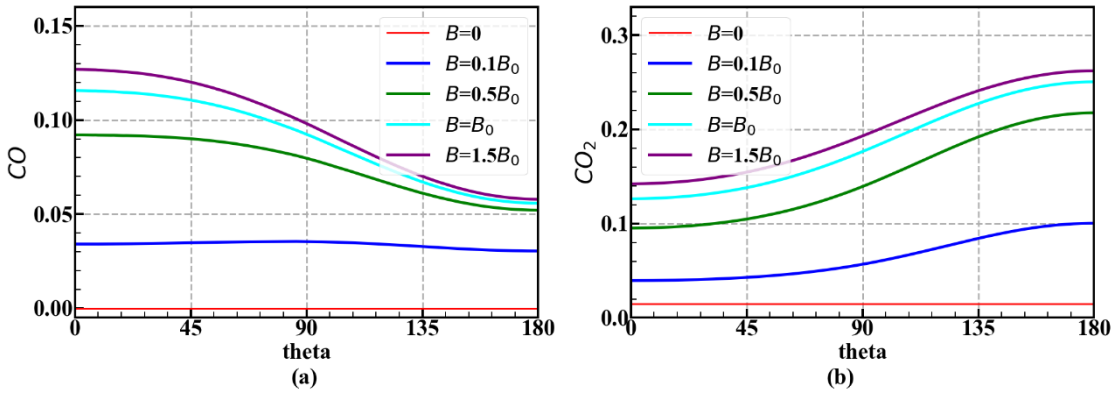

Fig. 6 Y_{CO} and Y_{CO2} profiles along the particle surface ($T_{particle}$=1500K, D_p=400μm, Re=5).

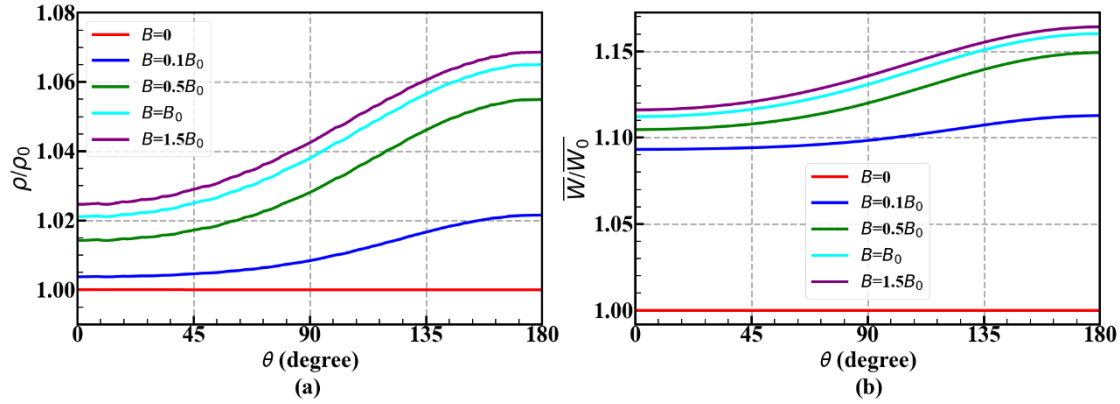

Fig. 7 Normalized density and molar mass distribution along the particle surface, $T_{particle}$=1500K, D_p=400μm, Re=5. (normalized by the density and molar mass of the incoming flow).

This is the accepted version of an article published in Combustion and Flame
http://dx.doi.org/10.1016/j.combustflame.2020.02.016

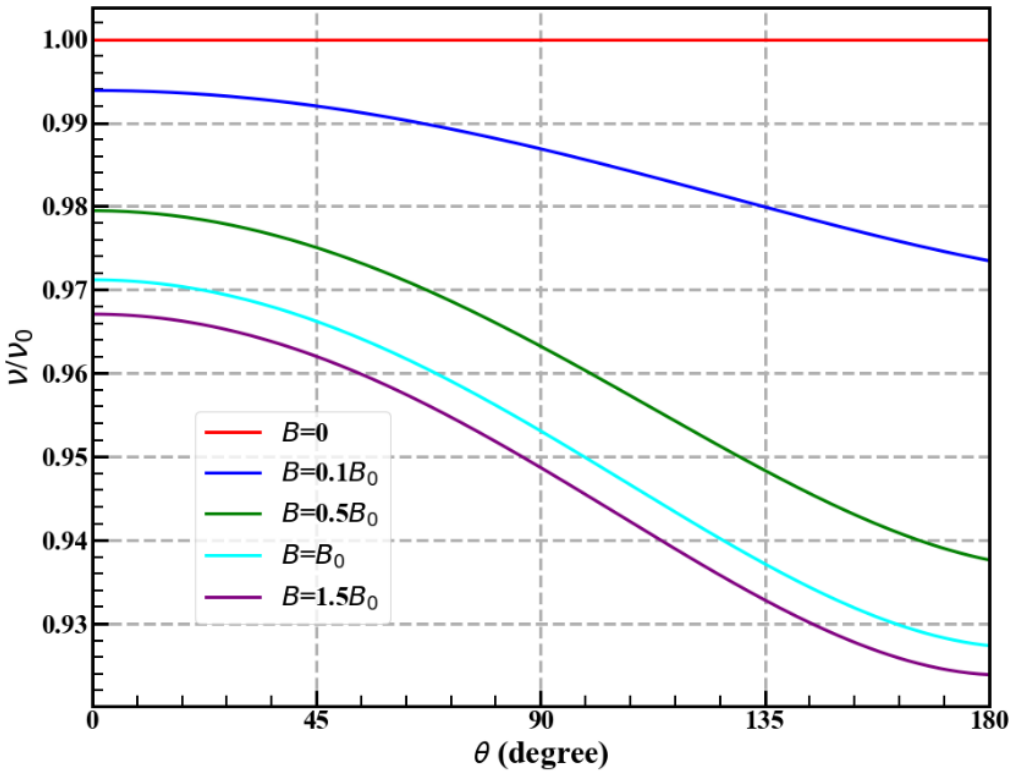

Fig. 8 Normalized kinematic viscosity coefficient distribution of particles with different reaction rates, normalized by the viscosity at the inlet ($T_{particle}$=1500K, D_p=400μm, Re=5).

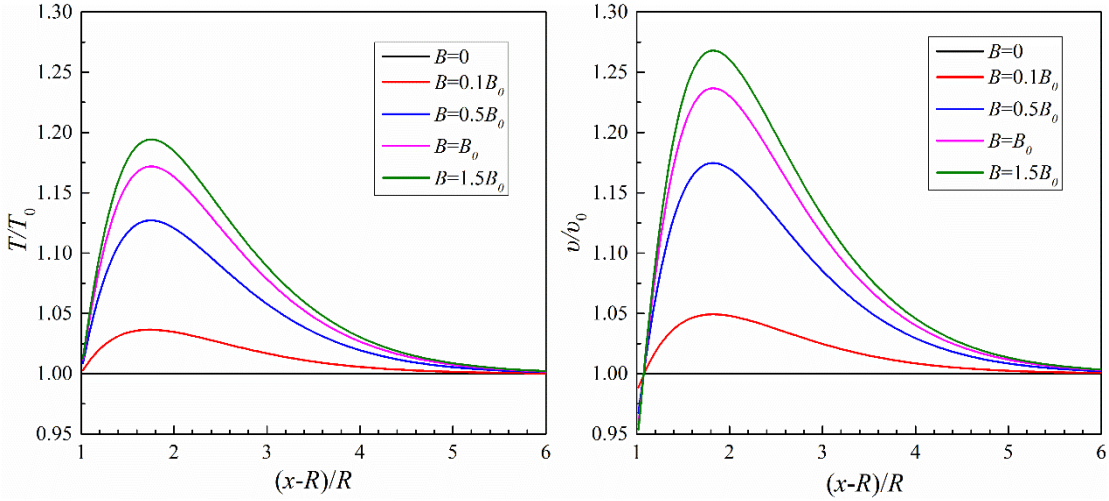

Fig. 9 Normalized temperature and kinematic viscosity coefficient (normalized by the value at the inlet) distribution as a function of normalized radial distance from the particle surface at θ=90° ($T_{particle}$=1500K, D_p=400μm, Re=5).

This is the accepted version of an article published in Combustion and Flame
http://dx.doi.org/10.1016/j.combustflame.2020.02.016

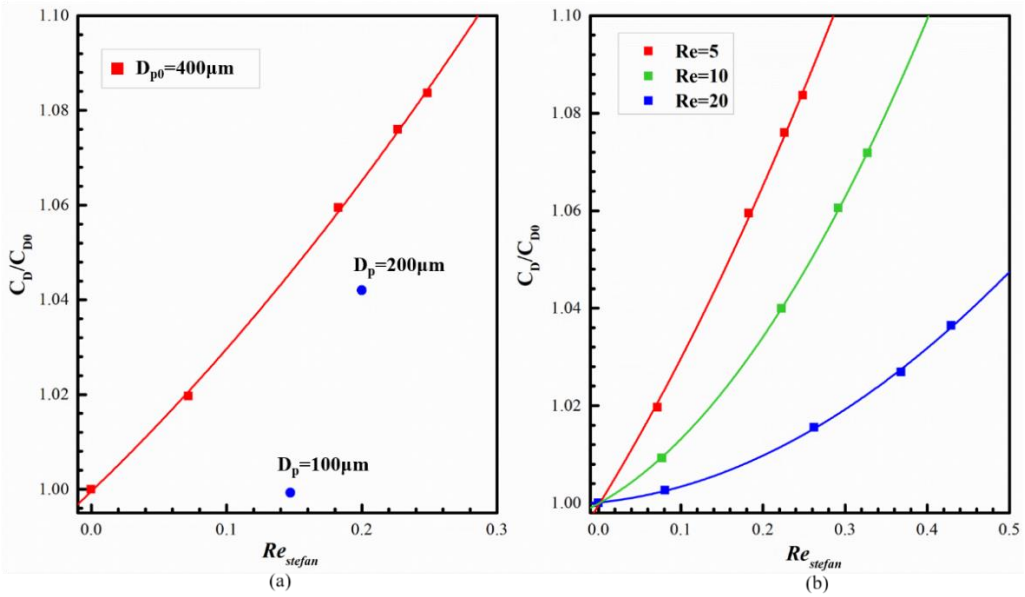

Fig. 10 (a) Drag force coefficients of particles with different diameters when Re=5 (b) Variation of drag force coefficients of different Reynolds numbers (solid lines are obtained using quadratic polynomial fitting)

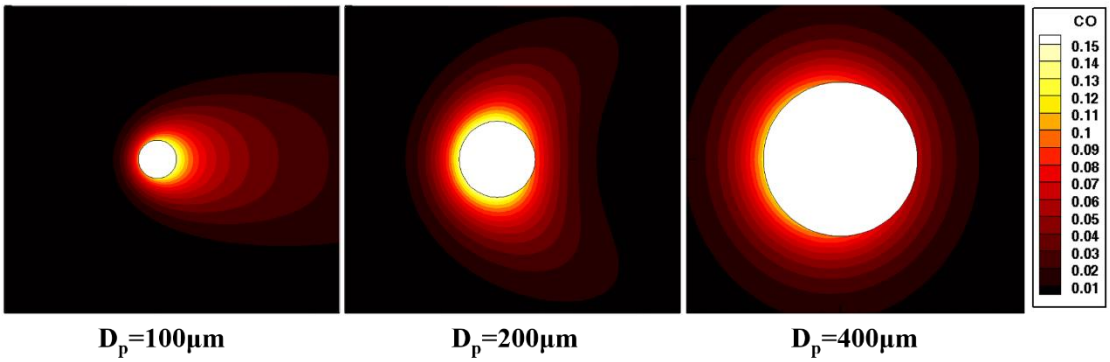

Fig. 11 Y_{CO} contours in the neighborhood of particles with different diameters ($T_{particle}$=1500K, Re=5, B=B_0)

This is the accepted version of an article published in Combustion and Flame
http://dx.doi.org/10.1016/j.combustflame.2020.02.016

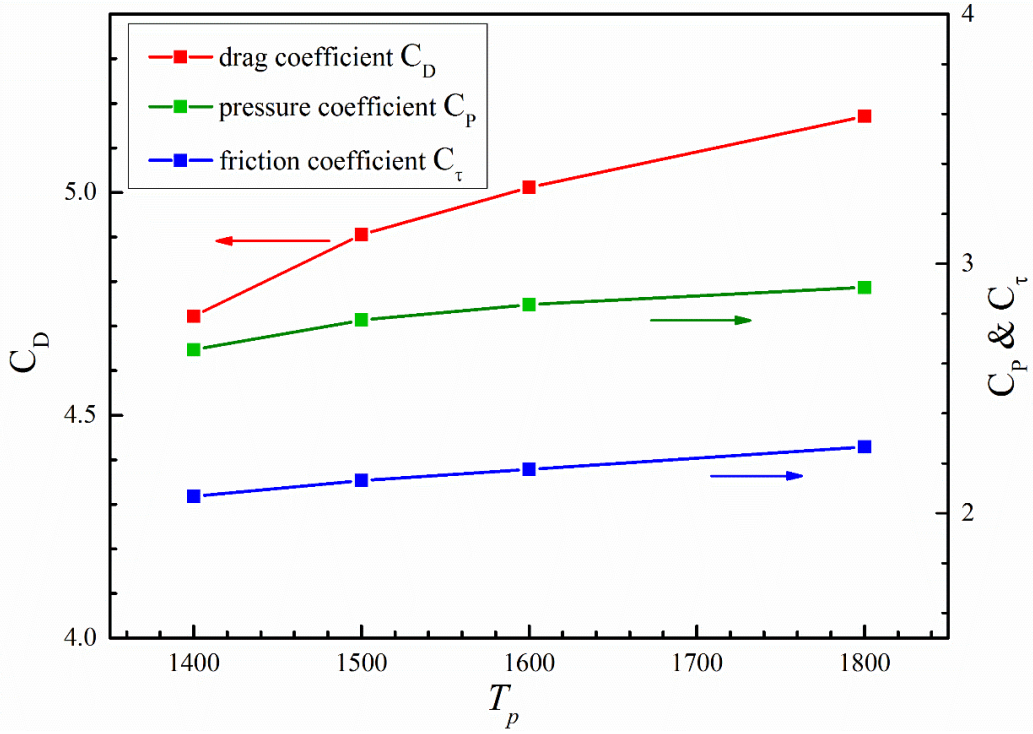

Fig. 12 Variation of drag force coefficients of reactive particles at different temperatures (D_p=400μm, Re=5, B=B_0)

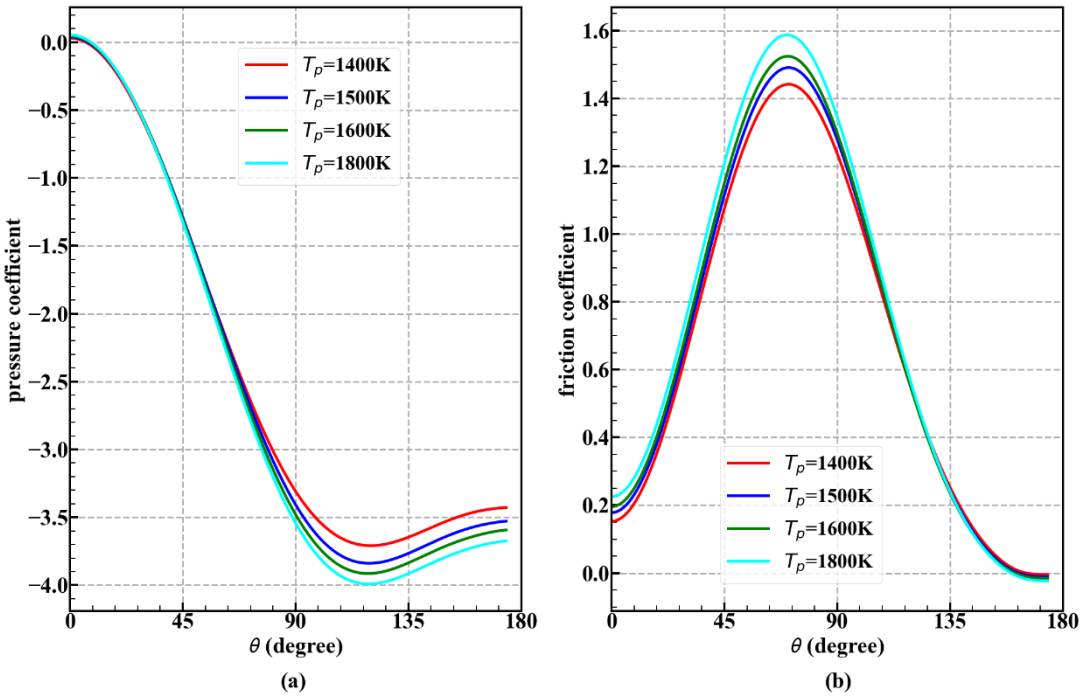

Fig. 13 Local pressure and friction coefficient distribution of particles with different temperatures (D_p=400μm, Re=5, B=B_0)

This is the accepted version of an article published in Combustion and Flame
http://dx.doi.org/10.1016/j.combustflame.2020.02.016

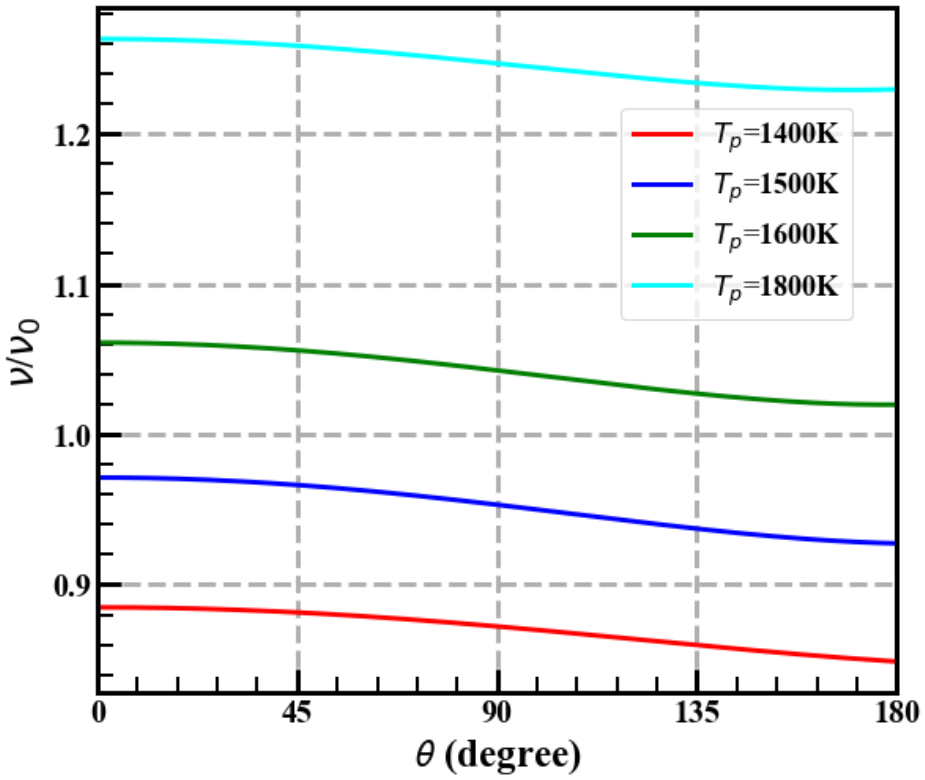

Fig. 14 Kinematic viscosity coefficient distribution of particles with different temperatures (D_p=400μm, Re=5, B=B_0)

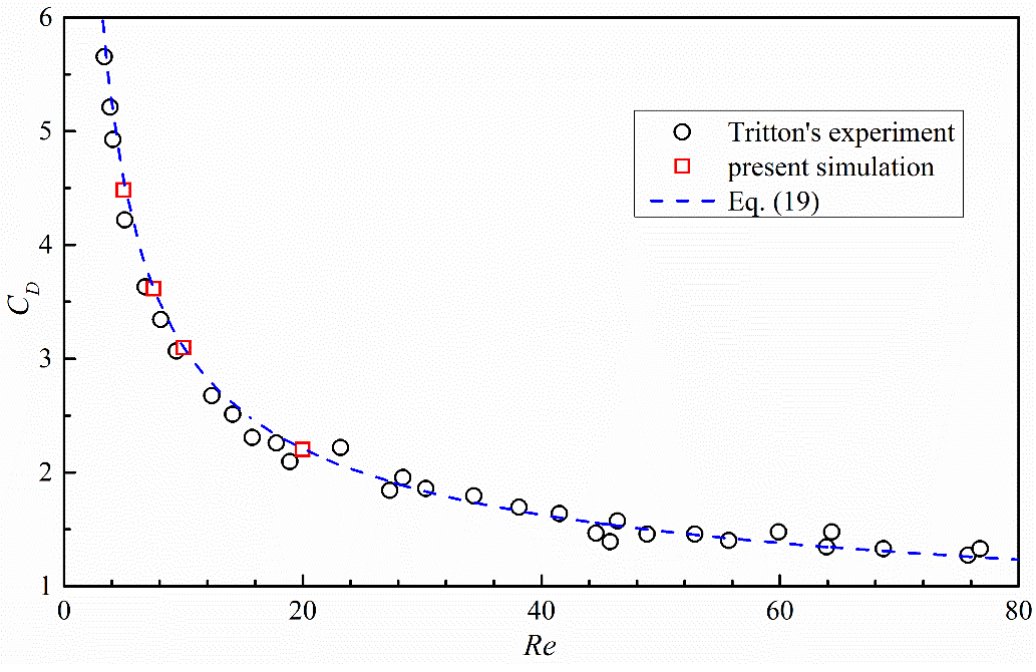

Fig. 15 Comparison of simulation data, experimental data [1], and Eq.(19)

This is the accepted version of an article published in Combustion and Flame
http://dx.doi.org/10.1016/j.combustflame.2020.02.016

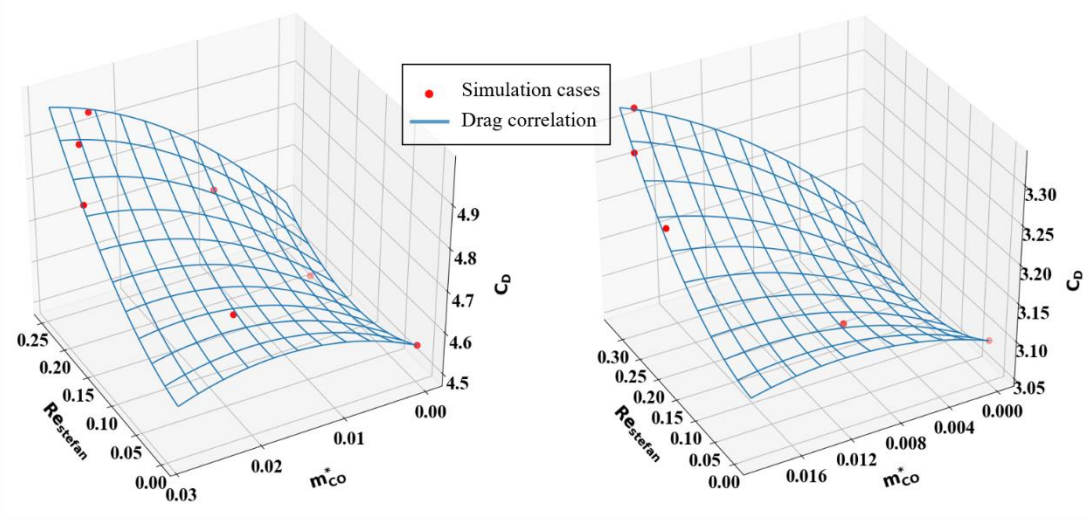

Fig. 16 Comparison of drag force of simulation cases and predicted drag force
(a) Re=5, (b) Re=10

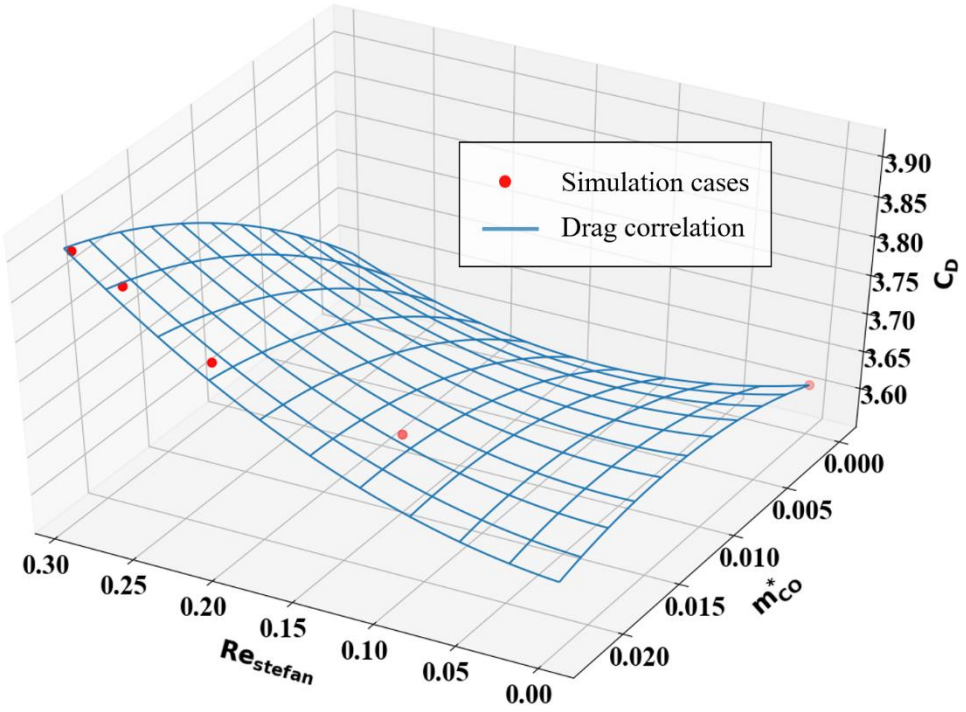

Fig. 17 Comparison of posterior analysis cases and predicted drag force

This is the accepted version of an article published in Combustion and Flame
http://dx.doi.org/10.1016/j.combustflame.2020.02.016

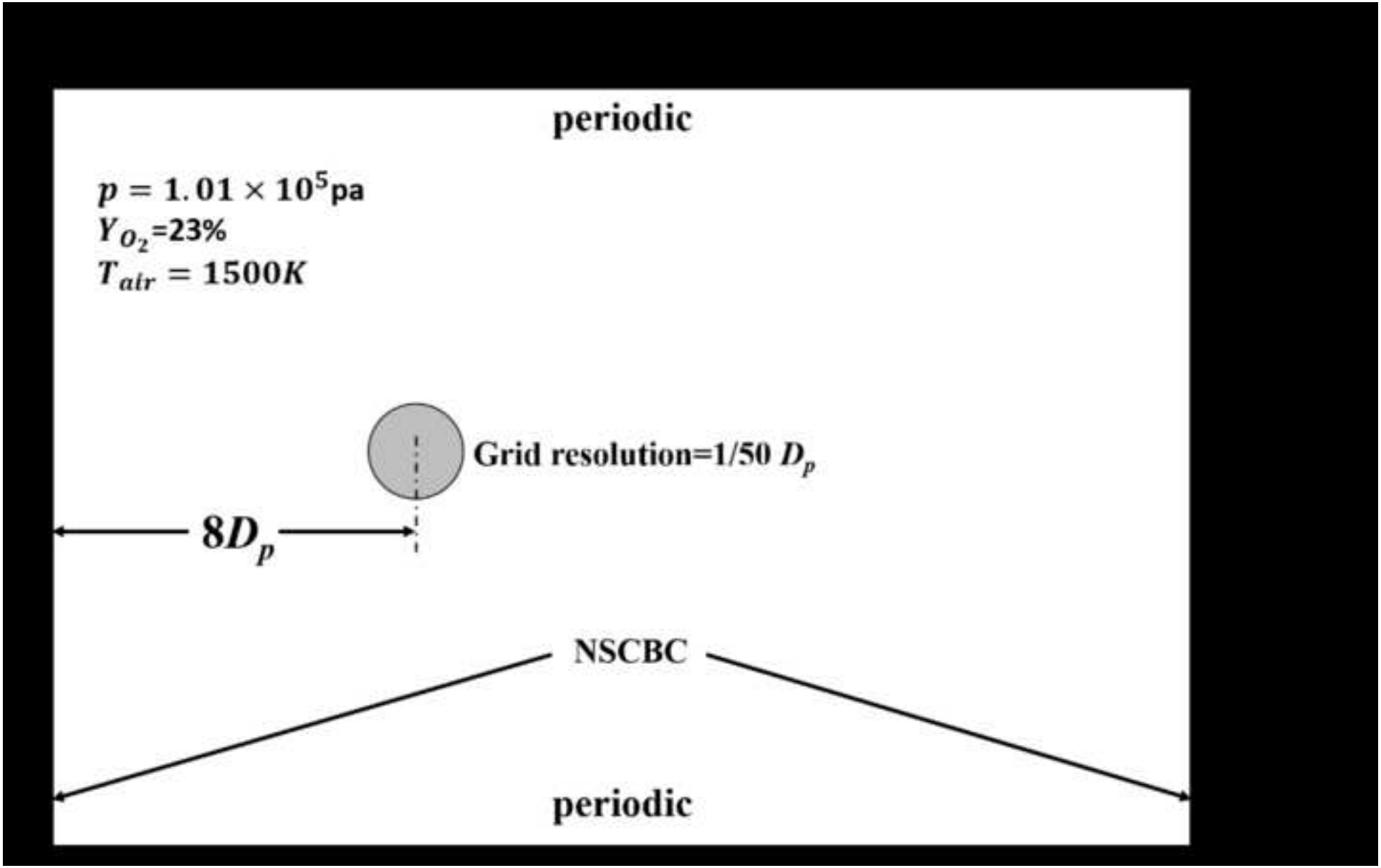

This is the accepted version of an article published in Combustion and Flame
http://dx.doi.org/10.1016/j.combustflame.2020.02.016

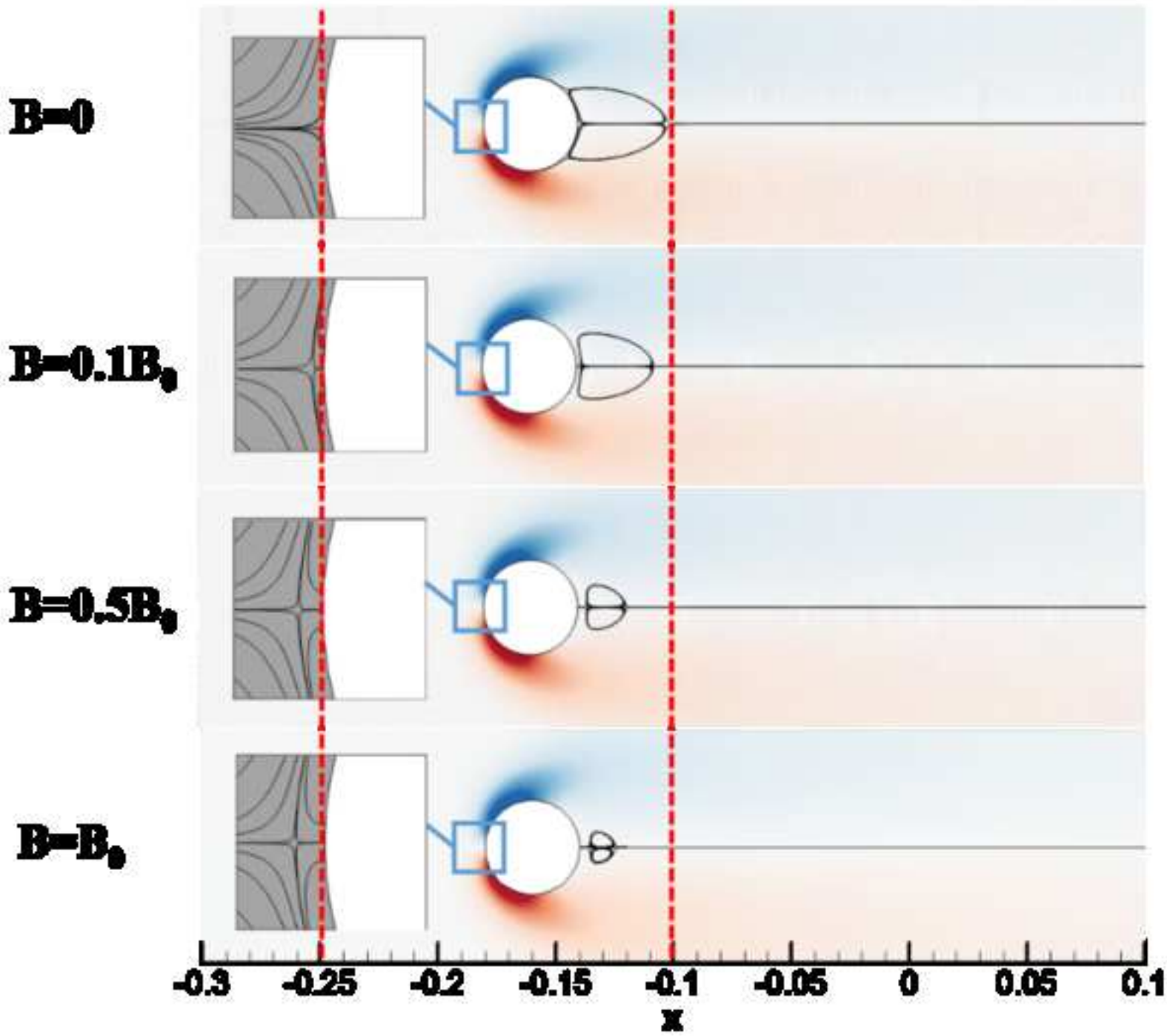

This is the accepted version of an article published in Combustion and Flame
http://dx.doi.org/10.1016/j.combustflame.2020.02.016

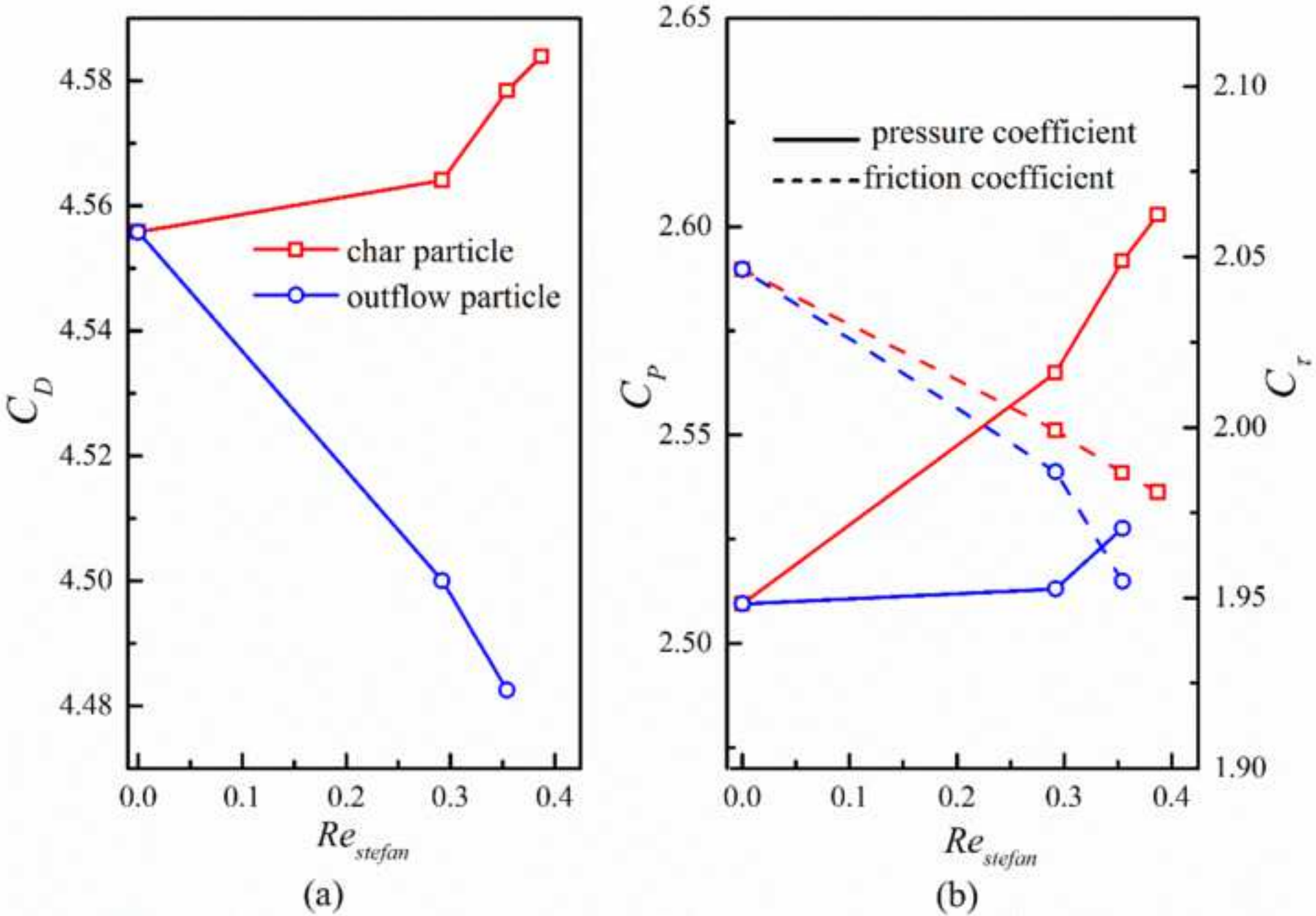

This is the accepted version of an article published in Combustion and Flame
http://dx.doi.org/10.1016/j.combustflame.2020.02.016

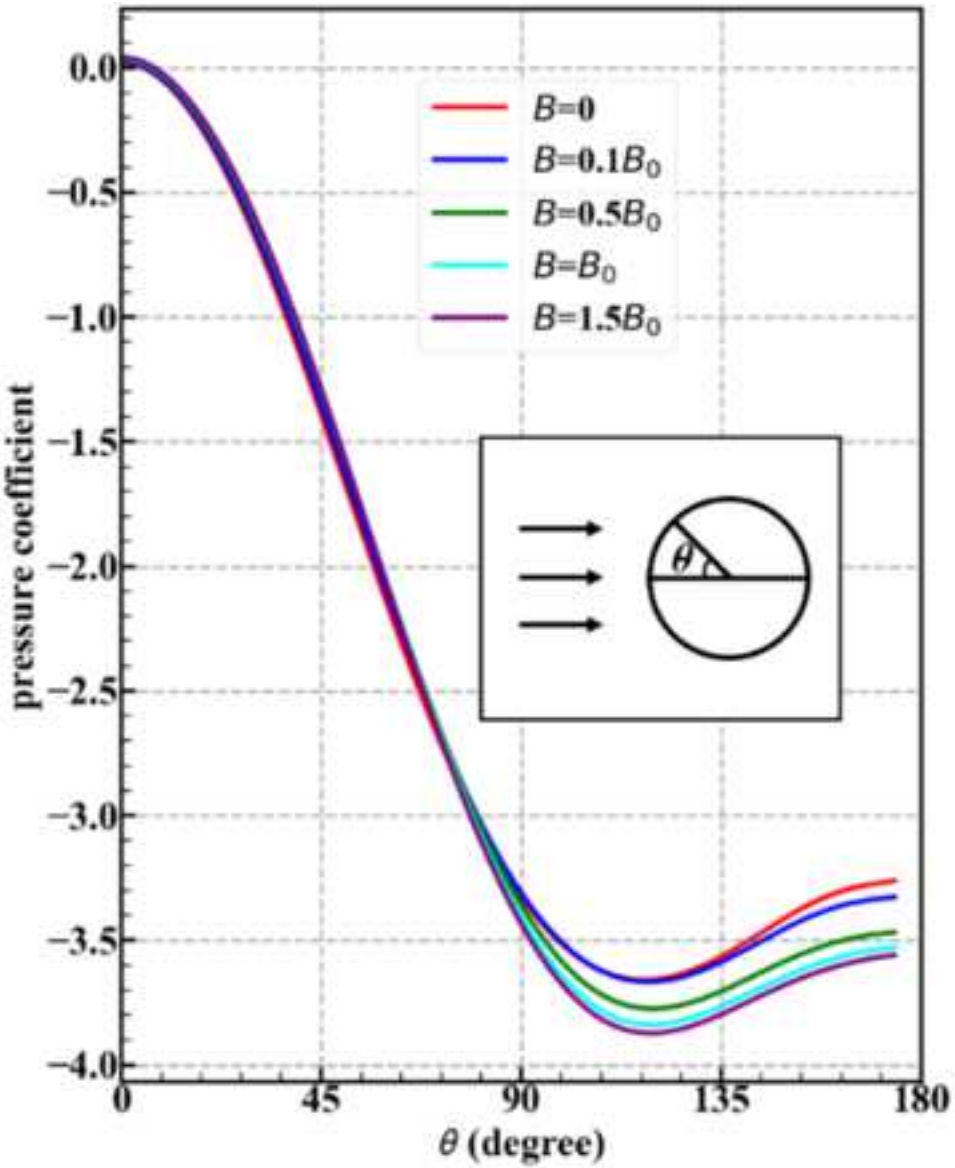

(a)

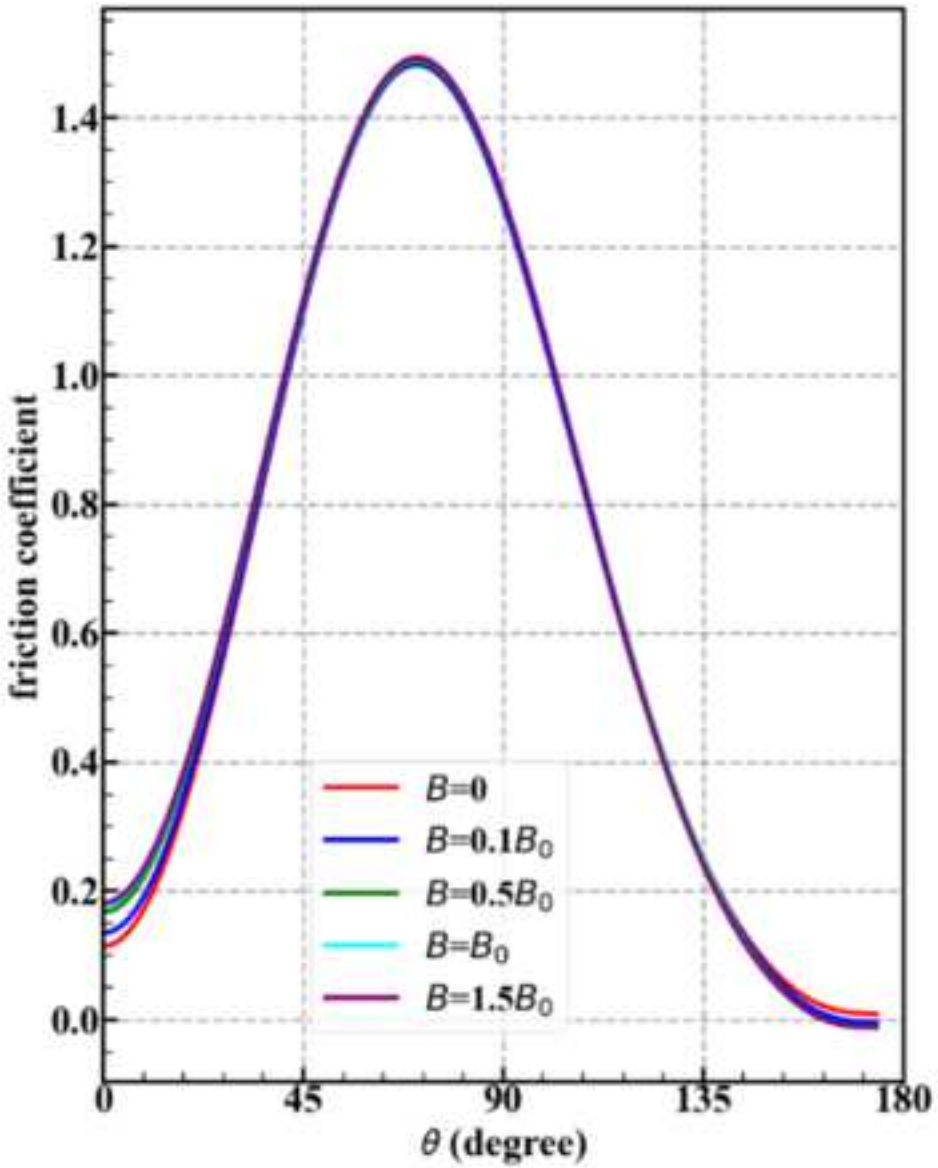

(b)

This is the accepted version of an article published in Combustion and Flame
http://dx.doi.org/10.1016/j.combustflame.2020.02.016

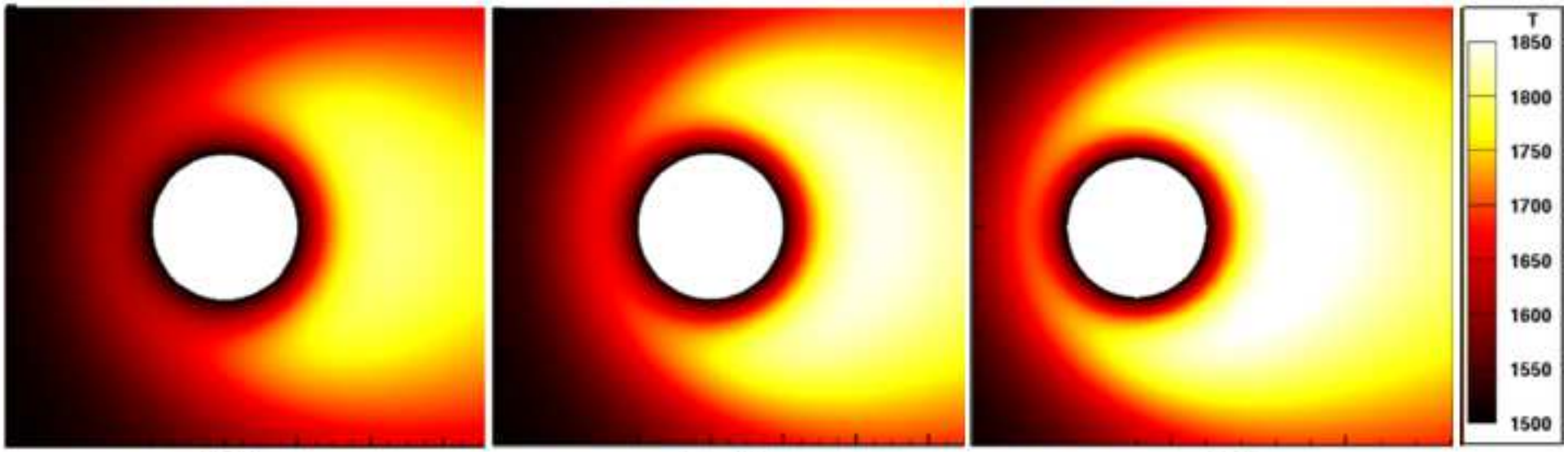

This is the accepted version of an article published in Combustion and Flame
http://dx.doi.org/10.1016/j.combustflame.2020.02.016

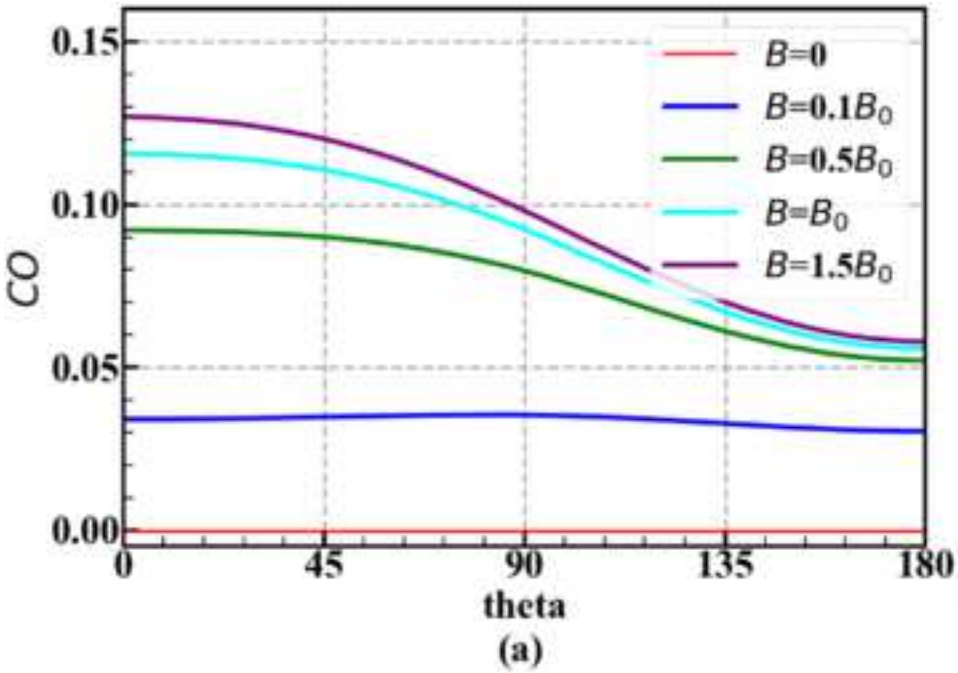

(a)

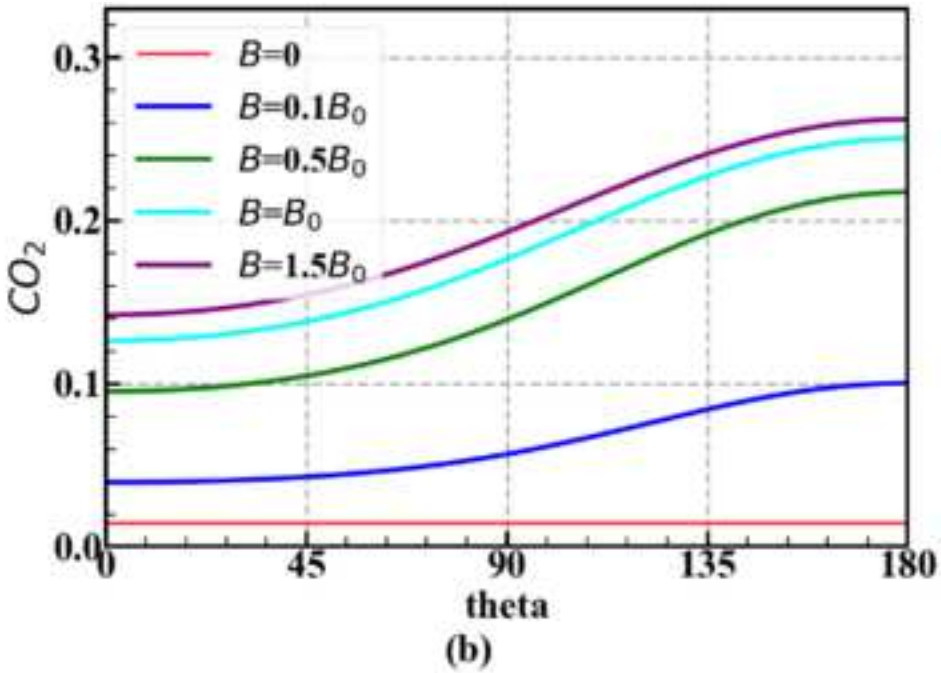

(b)

This is the accepted version of an article published in Combustion and Flame
http://dx.doi.org/10.1016/j.combustflame.2020.02.016

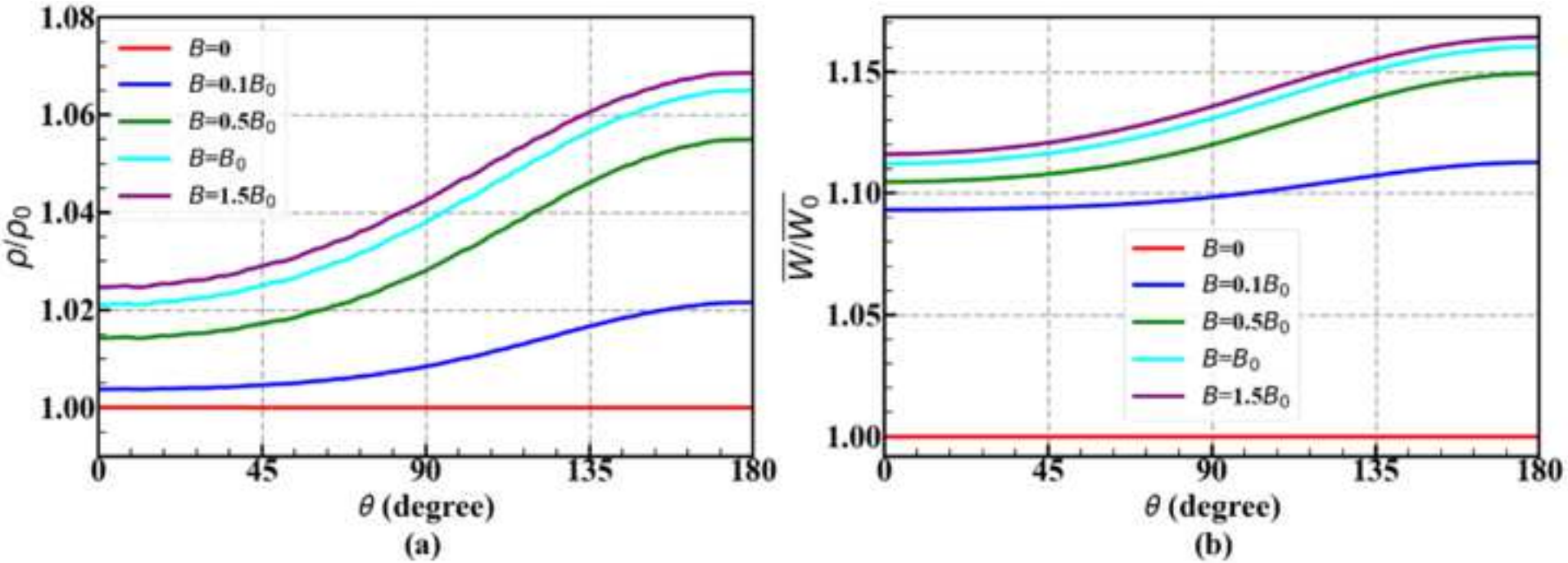

This is the accepted version of an article published in Combustion and Flame
http://dx.doi.org/10.1016/j.combustflame.2020.02.016

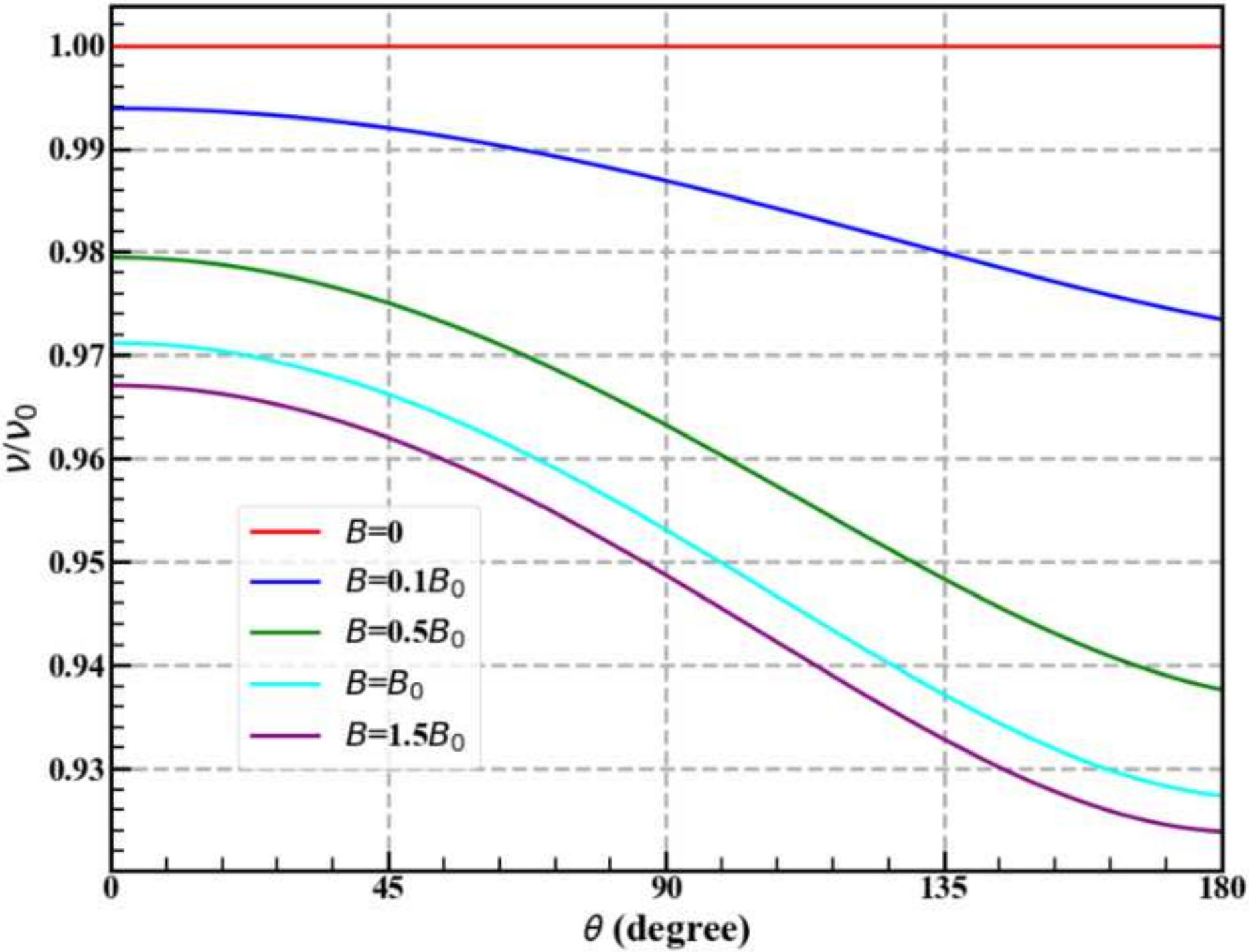

This is the accepted version of an article published in Combustion and Flame
http://dx.doi.org/10.1016/j.combustflame.2020.02.016

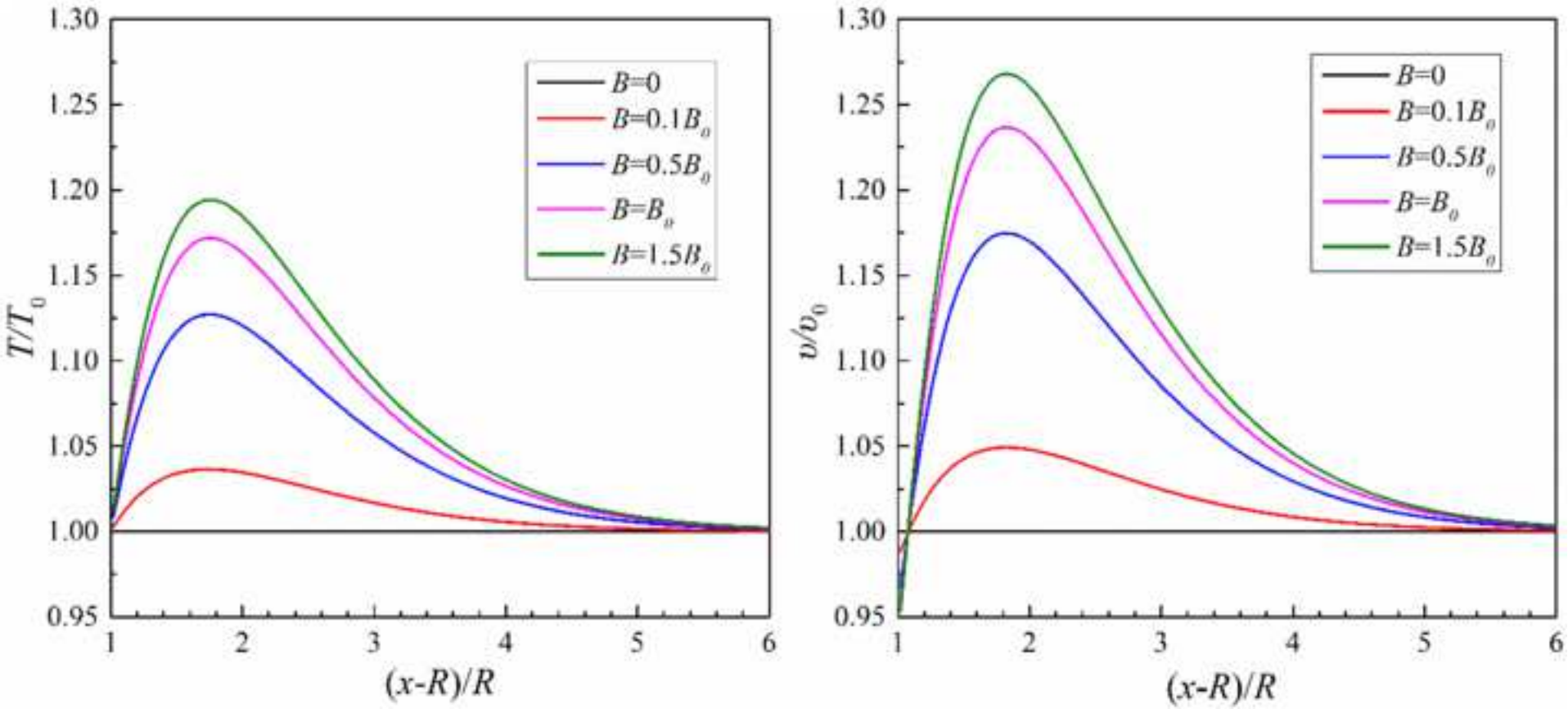

This is the accepted version of an article published in Combustion and Flame
http://dx.doi.org/10.1016/j.combustflame.2020.02.016

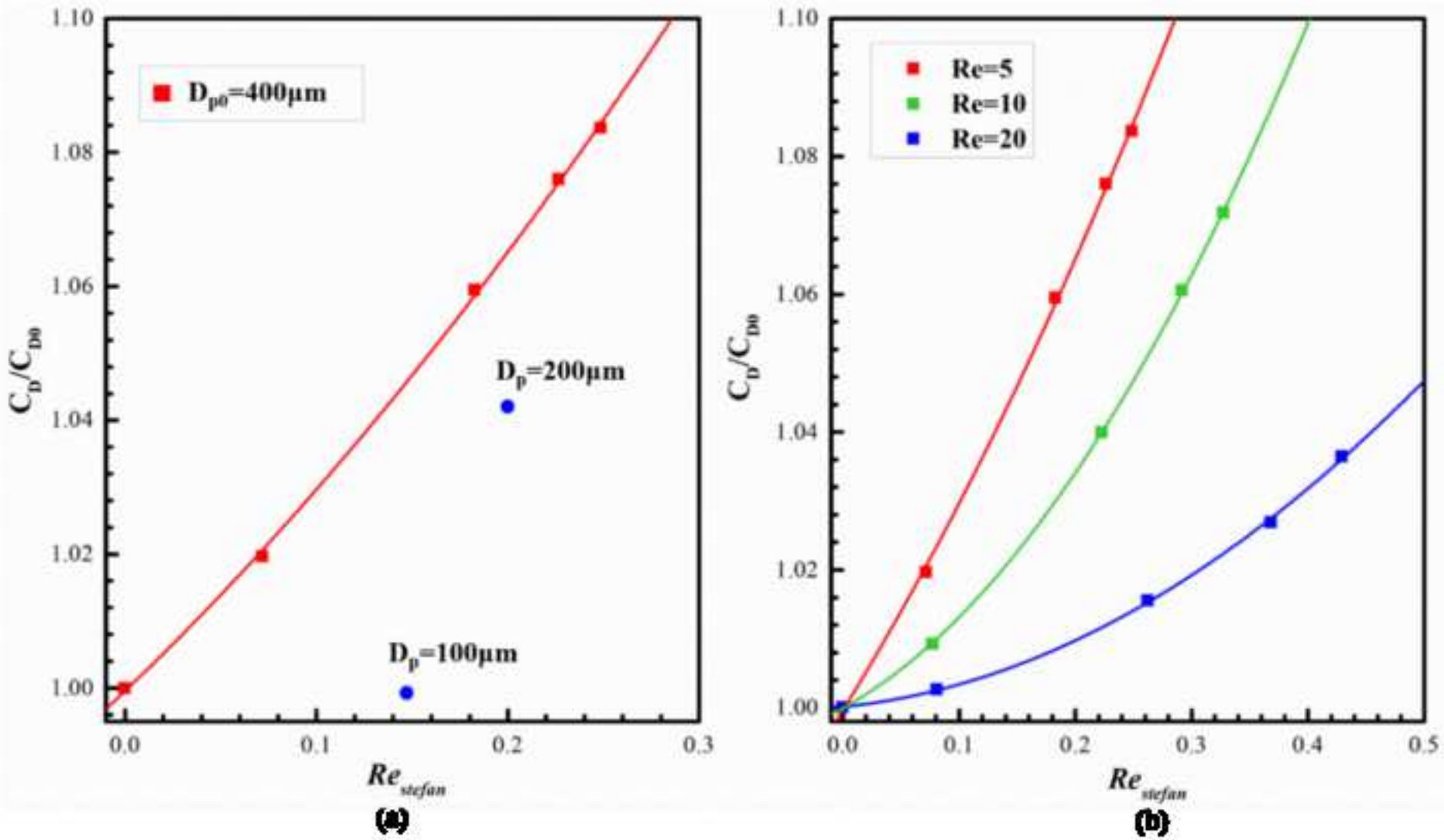

This is the accepted version of an article published in Combustion and Flame
http://dx.doi.org/10.1016/j.combustflame.2020.02.016

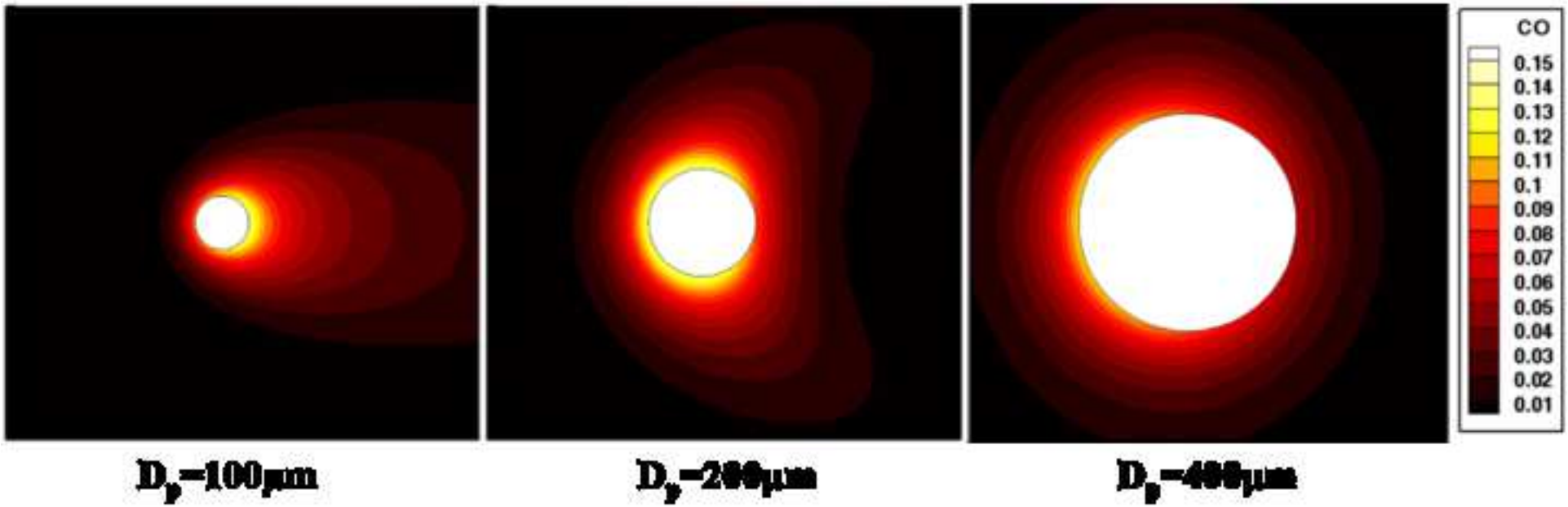

This is the accepted version of an article published in Combustion and Flame
http://dx.doi.org/10.1016/j.combustflame.2020.02.016

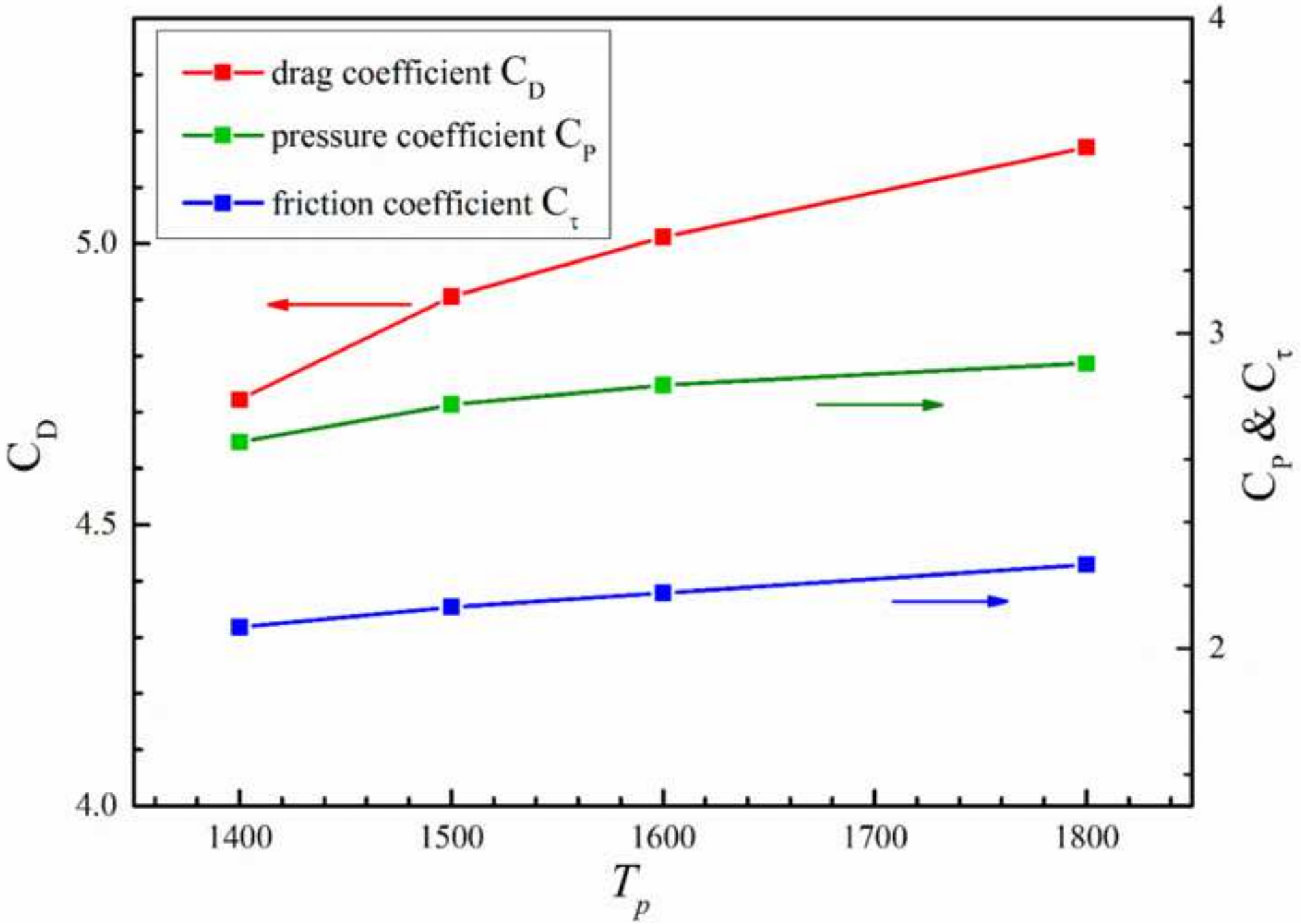

This is the accepted version of an article published in Combustion and Flame
http://dx.doi.org/10.1016/j.combustflame.2020.02.016

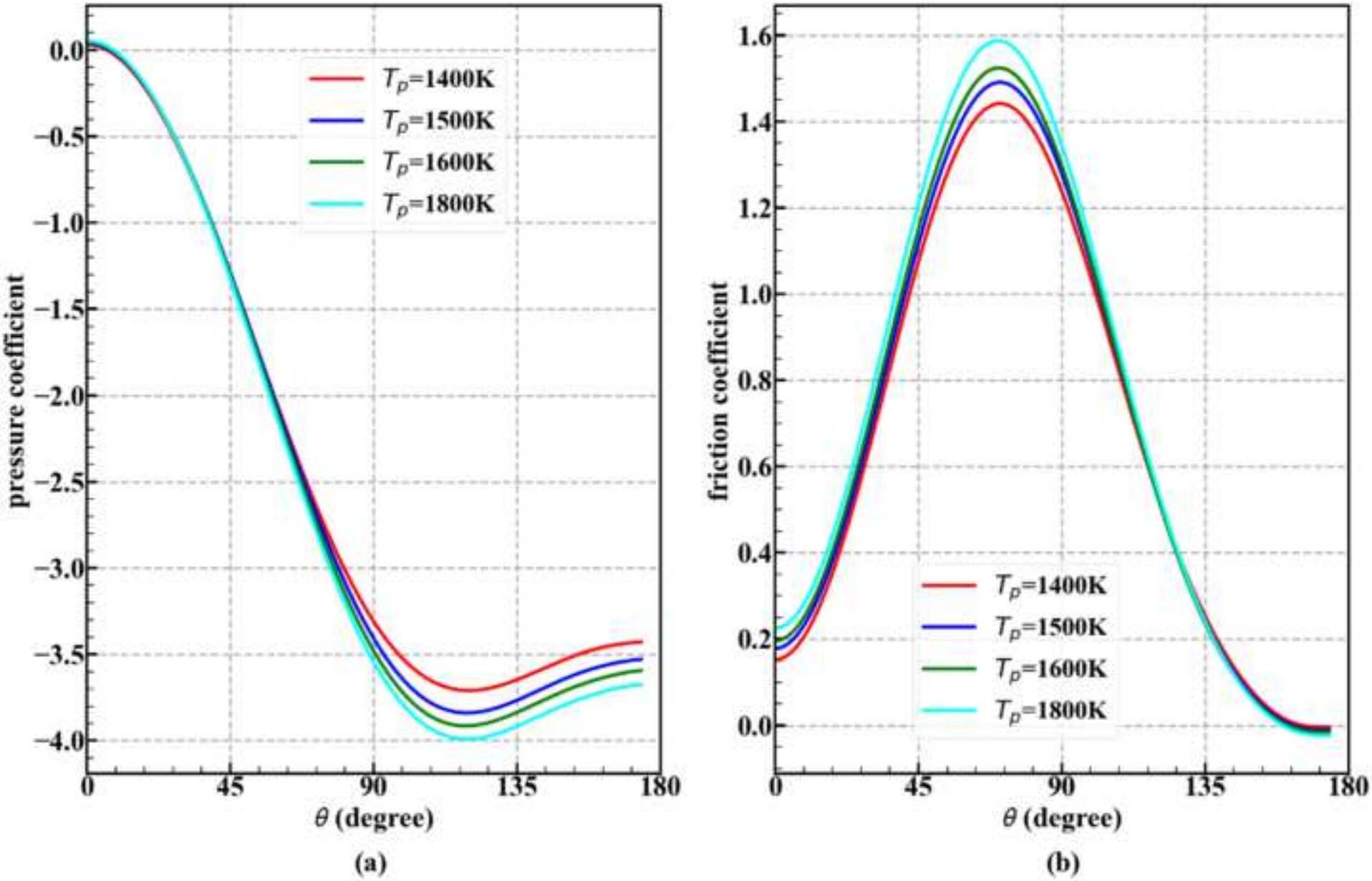

This is the accepted version of an article published in Combustion and Flame
http://dx.doi.org/10.1016/j.combustflame.2020.02.016

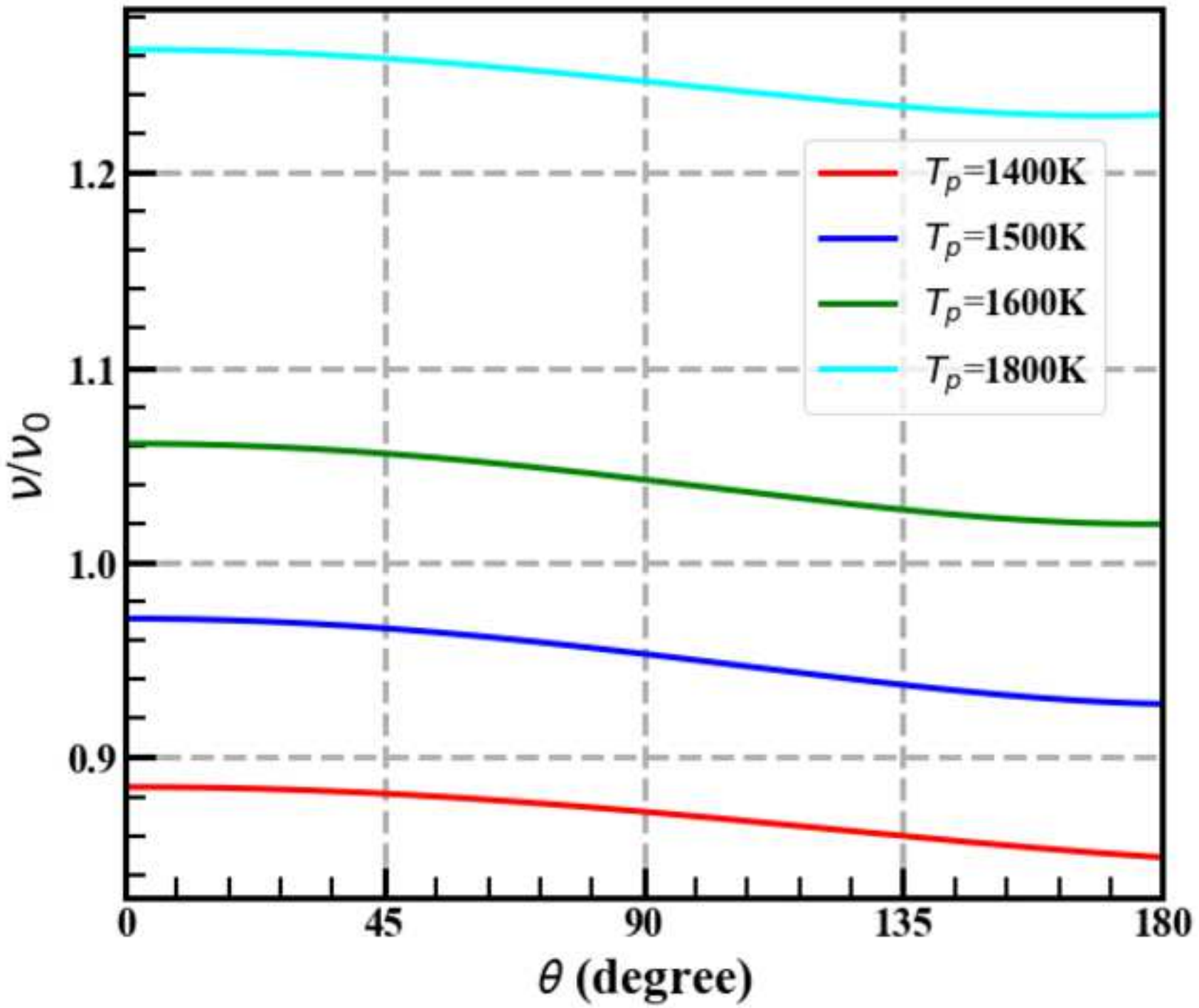

This is the accepted version of an article published in Combustion and Flame
http://dx.doi.org/10.1016/j.combustflame.2020.02.016

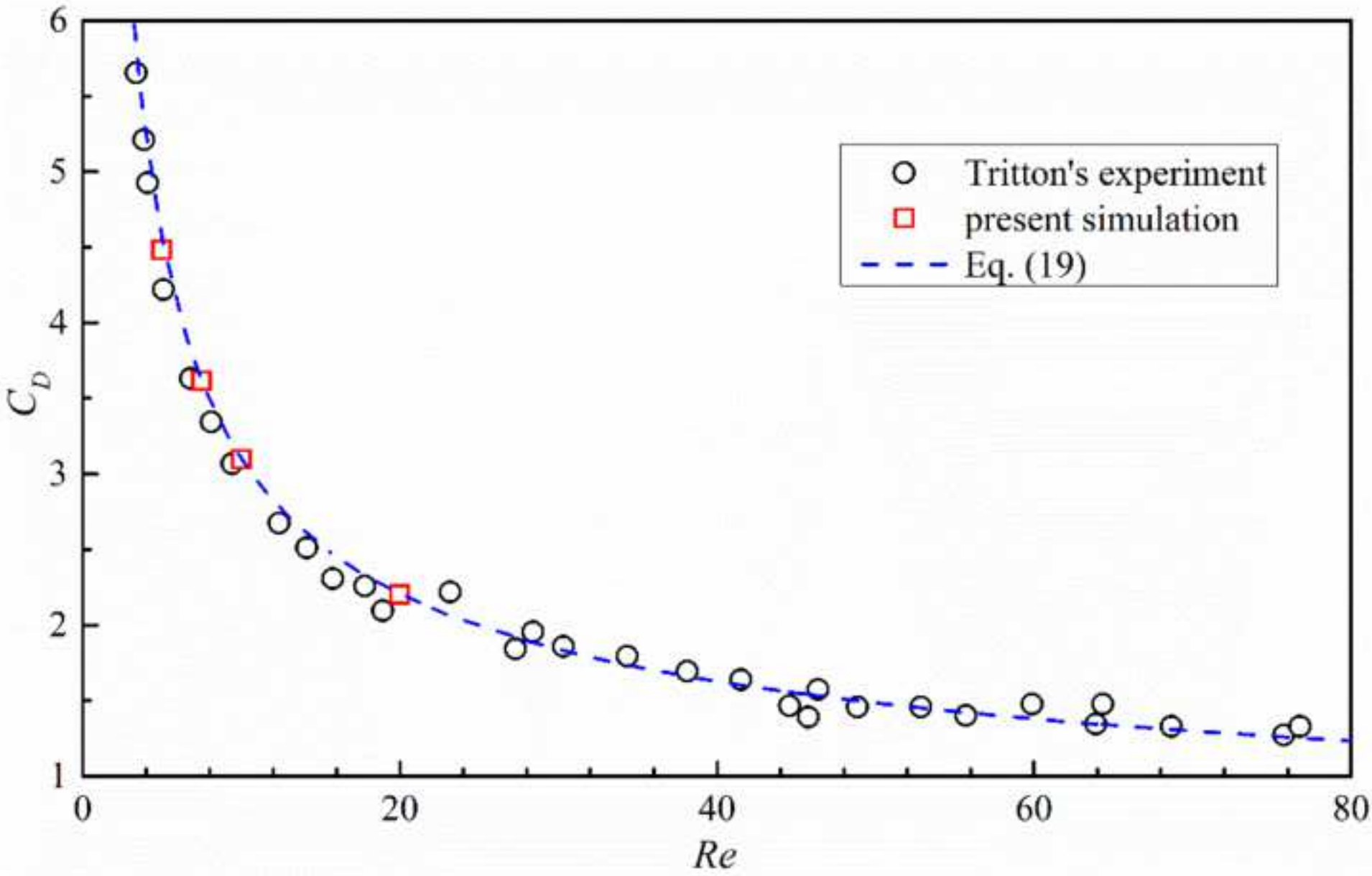

This is the accepted version of an article published in Combustion and Flame
http://dx.doi.org/10.1016/j.combustflame.2020.02.016

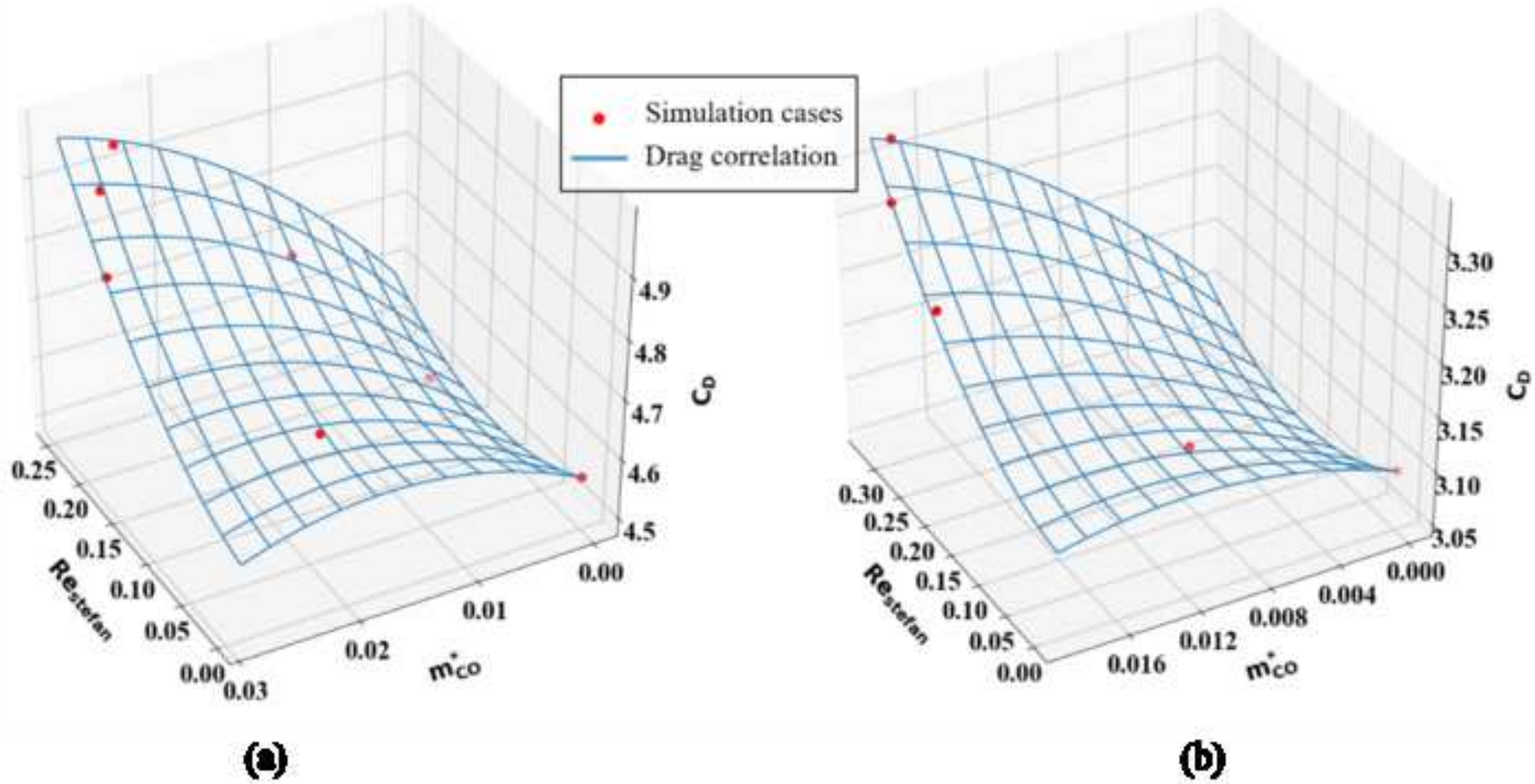

This is the accepted version of an article published in Combustion and Flame
http://dx.doi.org/10.1016/j.combustflame.2020.02.016

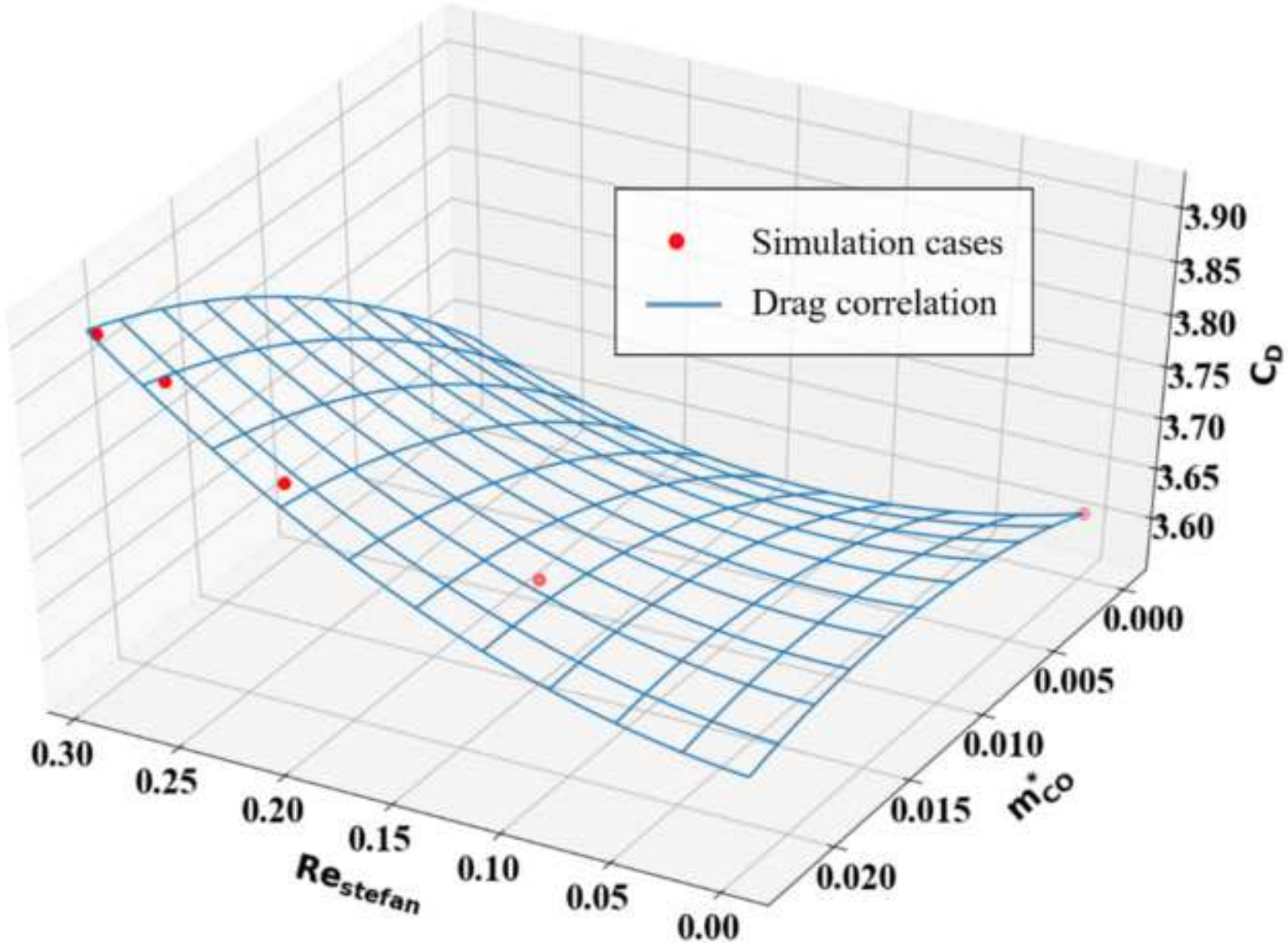

This is the accepted version of an article published in Combustion and Flame
http://dx.doi.org/10.1016/j.combustflame.2020.02.016

Declaration of Interest Statement

The authors have no conflicts of interest to declare.

This is the accepted version of an article published in Combustion and Flame
http://dx.doi.org/10.1016/j.combustflame.2020.02.016